The Astrophysical Journal, 908:8 (22pp), 2021 February 10 https://doi.org/10.3847/1538-4357/abd255


# The TW Hya Rosetta Stone Project. III. Resolving the Gaseous Thermal Profile of the Disk

Jenny K. Calahan[1], Edwin Bergin[1], Ke Zhang[1,2,17], Richard Teague[3], Ilsedore Cleeves[4], Jennifer Bergner[5], Geoffrey A. Blake[6], Paolo Cazzoletti[7], Viviana Guzmán[8], Michiel R. Hogerheijde[7,9], Jane Huang[1,3,18], Mihkel Kama[10,11], Ryan Loomis[12], Karin Öberg[3], Charlie Qi[3], Ewine F. van Dishoeck[7,13], Jeroen Terwisscha van Scheltinga[14,15], Catherine Walsh[16], and David Wilner[3]

[1] University of Michigan, 323 West Hall, 1085 South University Avenue, Ann Arbor, MI 48109, USA
[2] Department of Astronomy, University of Wisconsin–Madison, 475 N. Charter St., Madison, WI 53706, USA
[3] Center for Astrophysics | Harvard & Smithsonian, 60 Garden Street, Cambridge, MA 02138, USA
[4] Astronomy Department, University of Virginia, Charlottesville, VA 22904, USA
[5] University of Chicago, Department of the Geophysical Sciences, Chicago, IL 60637, USA
[6] Division of Chemistry & Chemical Engineering, California Institute of Technology, Pasadena, CA 91125, USA
[7] Leiden Observatory, Leiden University, 2300 RA Leiden, The Netherlands
[8] Instituto de Astrofísica, Ponticia Universidad Católica de Chile, Av. Vicuña Mackenna 4860, 7820436 Macul, Santiago, Chile
[9] Anton Pannekoek Institute for Astronomy, University of Amsterdam, The Netherlands
[10] Tartu Observatory, University of Tartu, Observatooriumi 1, 61602, Tõravere, Estonia
[11] Institute of Astronomy, University of Cambridge, Madingley Road, Cambridge CB3 0HA, UK
[12] National Radio Astronomy Observatory (NRAO), 520 Edgemont Rd., Charlottesville, VA 22903, USA
[13] Max-Planck-Institut für Extraterrestrische Physik, Giessenbachstrasse1, D-85748 Garching, Germany
[14] Leiden Observatory, Leiden University, P.O. Box 9513, 2300 RA Leiden, The Netherlands
[15] Laboratory for Astrophysics, Leiden Observatory, Leiden University, P.O. Box 9513, 2300 RA Leiden, The Netherlands
[16] School of Physics and Astronomy University of Leeds, Leeds LS2 9JT, UK
*Received 2020 May 19; revised 2020 December 8; accepted 2020 December 8; published 2021 February 8*

## Abstract

The thermal structure of protoplanetary disks is a fundamental characteristic of the system that has wide-reaching effects on disk evolution and planet formation. In this study, we constrain the 2D thermal structure of the protoplanetary disk TW Hya structure utilizing images of seven CO lines. This includes new ALMA observations of $^{12}$CO $J = 2$–1 and C$^{18}$O $J = 2$–1 as well as archival ALMA observations of $^{12}$CO $J = 3$–2, $^{13}$CO $J = 3$–2 and 6–5, and C$^{18}$O $J = 3$–2 and 6–5. Additionally, we reproduce a Herschel observation of the HD $J = 1$–0 line flux and the spectral energy distribution and utilize a recent quantification of CO radial depletion in TW Hya. These observations were modeled using the thermochemical code RAC2D, and our best-fit model reproduces all spatially resolved CO surface brightness profiles. The resulting thermal profile finds a disk mass of 0.025 $M_{\odot}$ and a thin upper layer of gas depleted of small dust with a thickness of ∼1.2% of the corresponding radius. Using our final thermal structure, we find that CO alone is not a viable mass tracer, as its abundance is degenerate with the total $H_2$ surface density. Different mass models can readily match the spatially resolved CO line profiles with disparate abundance assumptions. Mass determination requires additional knowledge, and, in this work, HD provides the additional constraint to derive the gas mass and support the inference of CO depletion in the TW Hya disk. Our final thermal structure confirms the use of HD as a powerful probe of protoplanetary disk mass. Additionally, the method laid out in this paper is an employable strategy for extraction of disk temperatures and masses in the future.

*Unified Astronomy Thesaurus concepts:* Protoplanetary disks (1300); Astrochemistry (75)

*Supporting material:* data behind figure

## 1. Introduction

The radial and vertical (2D) thermal profile of a gaseous protoplanetary disk is difficult to uncover but has wide-reaching effects on the physics, chemistry, and thus the planet formation potential of a disk. Further, temperature is often essential for estimation of other fundamental disk properties, such as the local sound speed and disk mass (Bergin & Williams 2017). Any physical process that relies on sound speed will also be affected by temperature. Turbulent viscosity, as one example, relies on sound speed and plays an important role in the transportation and redistribution of disk material (Shakura & Sunyaev 1973). The vertical density structure, in addition to the radial dependence, gives rise to the flaring of the disk and is highly dependent on the thermal structure (Kenyon & Hartmann 1995). In turn, the level of flaring sets the angle of incidence to stellar irradiation, producing strong vertical thermal gradients that lead to density profiles that deviate significantly from the derived Gaussian density profiles from assuming a vertically isothermal disk (Aikawa et al. 2002; Woitke et al. 2009; Gorti et al. 2011).

Temperature is also a determinate parameter to chemical processes. The gas temperature influences the rate of gas-phase exothermic reactions and, in particular, reactions that possess a significant activation barrier. Further, the midplane temperature controls the balance between gas-phase deposition and sublimation and thus the relative spatial composition of ices. For example, $H_2O$ freezes out at dust temperatures lower than ≈120–170 K (Fraser et al. 2001; Bergin & Cleeves 2018), while CO freezes out below ∼21–25 K in TW Hya, (Bisschop et al. 2006; Fayolle et al. 2016; Schwarz et al. 2016; Zhang et al. 2017). Thus, the gas/ice transition or snowline for water

[17] NASA Hubble Fellow.
[18] NHFP Sagan Fellow.

and CO is set by the thermal structure with water close to the star and CO at greater distances. Temperature-dependent snowlines are theorized to potentially be favorable sites for planet formation (Hayashi 1981; Stevenson & Lunine 1988; Zhang et al. 2015; Schoonenberg & Ormel 2017). Further, across various snowlines of key elemental carriers, the relative chemical composition of the disk changes the gas/solid state balance of these carriers, which will directly influence the chemical composition of planetary atmospheres or cores at birth (e.g., C/O ratio, Öberg et al. 2011; Öberg & Bergin 2016).

Temperature is also essential in estimating one of the most fundamental properties of a protoplanetary disk: its mass. Assuming a constant mass ratio between gas and dust and a dust mass opacity, submillimeter thermal continuum emission is generally used as an approximate tracer for the gas mass (Bergin & Williams 2017). However, this estimation is subject to large uncertainty, as grain evolution alters the dust opacity, both spatially and temporally; compounding the issue, the growth to pebble sizes and larger renders a large fraction of the solids inemissive at submillimeter wavelengths and essentially undetectable (Andrews 2020). CO emission provides an alternative method to estimate the gas mass, as CO has long been used as a tracer of $H_2$ mass in molecular clouds. However, the conversion of line emission to column density requires a prior knowledge of the temperature, CO distribution, and opacity to account for the fact that observations generally only sample the upper-state column of one rotational state. The CO abundance relative to $H_2$ remains relatively consistent throughout the dense interstellar medium (ISM) at approximately $10^{-4}$ relative to $H_2$ (Frerking et al. 1982; Lacy et al. 1994; Bergin & Williams 2017; Lacy et al. 2017). In protoplanetary disks, however, CO appears to be physically depleted, and such depletion varies not only disk by disk (Ansdell et al. 2016; Long et al. 2017; Miotello et al. 2017) but also radially (Zhang et al. 2019, 2020a) and possibly temporally owing to chemical and physical evolution (Reboussin et al. 2015; Bosman et al. 2018; Cleeves et al. 2018; Eistrup et al. 2018; Krijt et al. 2018; Schwarz et al. 2019; Zhang et al. 2020b). All of these factors complicate the use of CO to provide a reliable estimate of the total gas mass.

HD is a promising mass tracer, as the ratio of $HD/H_2$ is well calibrated via measurements of the atomic D/H ratio (Linsky 1998). However, the conversion of emission of HD to mass is strongly temperature sensitive for typical temperatures between 20 and 50 K; this is due to the first rotational state ($J = 1$–0) having an $E_{up}$ equal to 128.5 K above the ground (Bergin et al. 2013; Bergin & Williams 2017; Kama et al. 2020). A well-constrained disk mass derived using HD can only be determined if an accurate thermal structure is available (Trapman et al. 2017; Kama et al. 2020).

Given the wide-reaching impact of the thermal structure of a protoplanetary disk, it has long been a property sought after. Before the advent of the Atacama Large Millimeter/submillimeter Array (ALMA), the spectral energy distribution (SED) and spatially unresolved gas observations provided the best available constraints for most disks. One of the first attempts to uncover a thermal structure with single-dish observations was van Zadelhoff et al. (2001), which utilized isotopologues of CO, $HCO^+$, and HCN. By measuring the ratios of flux, they extrapolated densities and temperatures from which that flux originated. But with unresolved observations, spatial information becomes degenerate, as each of the isotopologues can be sensitive to different radial and vertical layers in the disk (Gorti et al. 2011; Zhang et al. 2017; Woitke et al. 2019). Spectrally resolved observations of isotopologues have already been illuminating, shedding light onto the thermal profiles of a handful of disks, e.g., Fedele et al. (2016), which utilized both spectrally resolved and unresolved lines of high-$J$ CO to extract thermal profiles of disks. While spatially unresolved, the spectrally resolved observations still can extract spatial information from the Keplerian rotation, if the disk inclination is known.

Spatially resolved observations allow for measurements of column densities and temperature information at different disk radii (Bruderer et al. 2012; Rosenfeld et al. 2013; Schwarz et al. 2016; Zhang et al. 2017; Pinte et al. 2018), providing finer constraints in a forward modeling approach. Kama et al. (2016) was one of the first to derive a thermal structure using a spatially resolved line, using CO 3–2 toward TW Hya. This resolved line in addition to much of the CO ladder produced improvements to the understanding of the TW Hya thermal profile. Toward IM Lup, Pinte et al. (2018) observed the 2–1 transition of $^{12}CO$, $^{13}CO$, and $C^{18}O$ and directly extrapolated $T_{gas}$ from spatially resolved optically thick lines, independent of any modeling.

The thermal structure of TW Hya has been probed using its SED in concert with a large array of spatially unresolved lines, including various transitions of CO, $HCO^+$, and $H_2O$ (van Zadelhoff et al. 2001; Gorti et al. 2011; Zhang et al. 2017; Woitke et al. 2019). Often these thermal profiles were empirically derived using these observations. With new thermochemical models that take into account radiative transfer and chemical evolution, the disk thermal structure can be derived using a forward modeling approach by reproducing observations (Woitke et al. 2019) including spatially resolved lines, providing finer insight into radial structure (Kama et al. 2016). The goal of this paper is to lay out a new approach to uncover a gaseous protoplanetary disk thermal profile by utilizing multiple spatially resolved observations. Using a thermochemical code, we aim to reproduce seven spatially resolved CO line observations toward the class II, nearby (60 pc; Bailer-Jones et al. 2018; Gaia Collaboration et al. 2018), face-on TW Hya disk. It is worth noting that we do not seek to reproduce scattered-light or continuum observations. While these observations provide additional constraints on the temperature structure (more directly on the dust temperature and indirectly on gas temperature), a detailed dust model would require further assumptions on how dust properties vary with radius (Huang et al. 2018), as well as assumptions on dust scattering, which add uncertainty in dust temperature determinations (Zhu et al. 2019). Such simulated observations would be nontrivial with our current model, and the goal of this paper is to uncover the broader gaseous thermal profile and mass. While continuum and scattered-light images provide insight into deviations from a smooth density distribution, that information may not translate into an effect on the gas density and temperature.

The present study uses data from the TW Hya Rosetta Stone Project (PI: Cleeves), along with other archival data sets. The complete set of observations, including the CO and isotopologue maps from Schwarz et al. (2016) and Huang et al. (2018), span a wide range of optical depths, thereby tracing both the vertical and radial temperature simultaneously when observations are spatially resolved, in the case for optically thick

**Table 1**
ALMA Observations Summary

| Program ID | P.I. | Species and Transition | Frequency (GHz) | $E_{up}$[a] (K) | Beam (PA) (au × au) (deg) | $\sigma$[b] (mJy beam$^{-1}$) | $v_\sigma$[c] (km s$^{-1}$) | $I_{peak}$[d] (mJy beam$^{-1}$ km s$^{-1}$) | $F_{line}$[e] (Jy km s$^{-1}$) |
|---|---|---|---|---|---|---|---|---|---|
| 2016.1.00311.S | I. Cleeves | $^{12}$CO $J = 2$–1 | 230.538 | 16.6 | 22 × 16 [89.02] | 3.9 | 0.56 | 828 | 17.8 |
| 2015.1.00686.S | S. Andrews | $^{12}$CO $J = 3$–2 | 345.795 | 33.2 | 8.3 × 7.7 [−74.96] | 1.7 | 0.25 | 541 | 43.2 |
| 2016.1.00629.S | I. Cleeves | | | | | | | | |
| 2012.1.00422.S | E. Bergin | $^{13}$CO $J = 3$–2 | 330.587 | 15.9 | 30 × 18 [88.15] | 9.2 | 0.09 | 574 | 4.35 |
| 2012.1.00422.S | E. Bergin | $^{13}$CO $J = 6$–5 | 661.067 | 111.1 | 23 × 14 [−84.84] | 56 | 0.11 | 2248 | 8.21 |
| 2016.1.00311.S | I. Cleeves | C$^{18}$O $J = 2$–1 | 219.560 | 15.8 | 24 × 18 [87.65] | 3.2 | 0.10 | 66 | 0.57 |
| 2012.1.00422.S | E. Bergin | C$^{18}$O $J = 3$–2 | 329.331 | 31.6 | 30 × 18 [88.62] | 12 | 0.11 | 252 | 1.16 |
| 2012.1.00422.S | E. Bergin | C$^{18}$O $J = 6$–5 | 658.553 | 110.6 | 23 × 14 [−79.98] | 77 | 0.09 | 973 | 1.56 |

**Notes.**
[a] Müller et al. (2005).
[b] Rms noise—measured from line-free channels.
[c] Velocity width assumed in rms determination.
[d] Peak integrated intensity flux—errors are visualized in Figure 4.
[e] Total integrated flux, calculated within a circle with radius 4″ for $^{12}$CO 2–1 and 3–2, a circle with radius 2″ for C$^{18}$O 2–1 and 3–2 and $^{13}$CO 3–2, and a circle with radius 1″ for C$^{18}$O and $^{13}$CO 6–5 (see Figure 1). The error in the observed flux ranges from 10% to 15% based on the ALMA technical handbook.

molecules. Molecules that turn out to be optically thin will provide column density information. Additionally, we seek to reproduce the HD flux measured with Herschel and the SED of the disk.

We detail our ALMA observations in Section 2 and our modeling procedure in Section 3. In Section 4 we explore our best-fit thermal model to investigate possible model degeneracies. Comparisons to other models and the future of HD observations are explored in Section 5, and we summarize our findings in Section 6.

## 2. Observations

We present new observations of $^{12}$CO 2–1 and C$^{18}$O 2–1 taken as a part of the Rosetta collaboration. Archival ALMA data were also used for $^{12}$CO 3–2, C$^{18}$O 3–2 and 6–5, and $^{13}$CO 3–2 and 6–5. The archival HD 1–0 flux measurement from Herschel and SED fluxes from the literature were also used. A summary of all observations can be found in Table 1. Using BETTERMOMENTS[19] (Teague & Foreman-Mackey 2018), zero-moment maps were calculated for each of the CO observations described below and are presented in Figure 1. Each zero-moment map was then azimuthally averaged, producing the radial emission profiles. These radial profiles provided the constraints that we used below to determine the 2D thermal structure of TW Hya.

### 2.1. CO Observations from TW Hya Rosetta Project

We report new observations of $^{12}$CO 2–1 and C$^{18}$O 2–1 as part of the program 2016.1.00311.S (PI Cleeves). The compact observations (baselines down to 15 m) were obtained on 2016 December 16 in configuration C43-3 for a total on-source integration time of 81 minutes. The extended observations (baselines up to 1124 m) were carried out on 2017 May 5 and 7 in C43-6 with an on-source integration time of 25 minutes. The data were calibrated by the CASA pipeline (McMullin et al. 2007). For the extended observations, J1058+0133 and J1037–2934 were used as bandpass calibrators, J1107–4449 as the flux calibration, and J1037–2934 as the phase calibrator. For the compact observations, J1037–2934 was used for bandpass, flux, and phase calibration. We performed one additional round of phase self-calibration on each of the extended and compact observations independently using CASA version 4.5.0. For the self-calibration we adopted a solution interval of 30 s and averaged both polarizations. Spectral windows were not averaged in the self-calibration step, and the solutions were mapped to the individual spectral windows.

Each data cube was first centered to the same central coordinate, and then the continuum was subtracted from the line observations in the *u-v* plane using the CASA routine *uvcontsub*. The continuum-subtracted long and short baselines were then combined using the method *concat*, where the spectral windows that excluded the lines were manually specified. The images were produced in CASA version 4.6.12 using *tclean*, with Briggs weighting and a robust parameter of 0.5. The final spectral resolutions of CO and C$^{18}$O were 246.08 and 73.24 kHz, respectively. The C$^{18}$O restoring beam had FWHM dimensions of 0.″40 × 0.″30, and $^{12}$CO had 0.″37 × 0.″28.

### 2.2. Archival CO Data

The $^{12}$CO $J = 3$–2 analysis and imaging procedures are reported in Huang et al. (2018), and the $^{13}$CO $J = 3$–2 and 6–5 and C$^{18}$O $J = 3$–2 and 6–5 observations are described in Schwarz et al. (2016) and not repeated here. We utilize their final data reduction and images.

### 2.3. Spatially Unresolved Observations: HD Flux and SED

HD $J = 1$–0 was observed using Herschel, and the observed total integrated flux was $6.3(\pm 0.7) \times 10^{-18}$ W m$^{-2}$ (Bergin et al. 2013). The line is spatially unresolved; thus, we only use the integrated line flux to compare the models.

TW Hya is one of the most thoroughly observed protoplanetary disks in the literature, with a well-characterized SED. The main purpose of the SED is to constrain the thermally coupled small dust population. Data points for the SED were taken from Cleeves et al. (2015), which in turn used individual photometric measurements from the literature (Weintraub et al. 1989a, 2000; Mekkaden 1998; Wilner et al. 2000, 2003;

[19] https://github.com/richteague/bettermoments

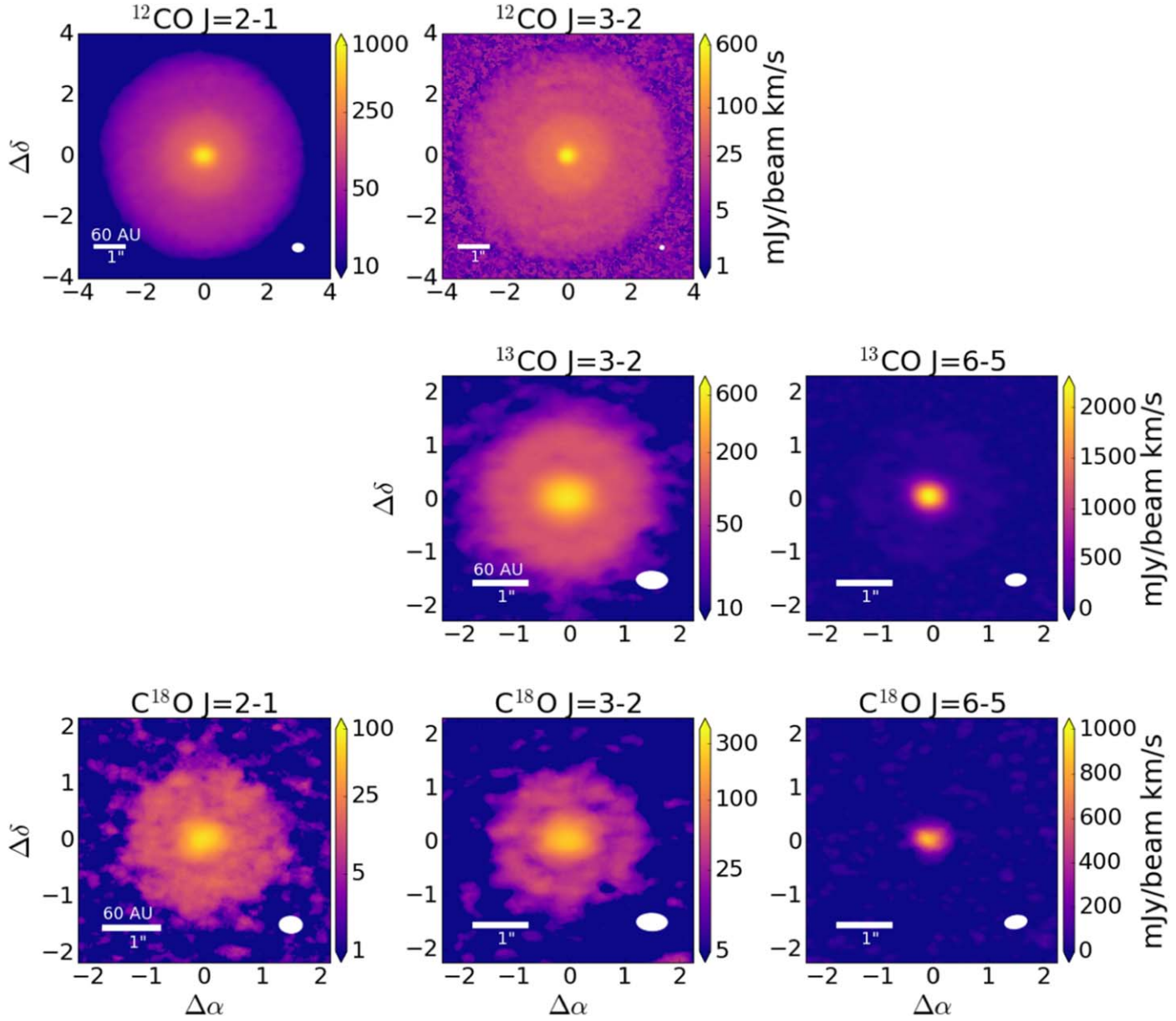


**Figure 1.** Integrated emission maps of TW Hya in $^{12}$CO $J = 2$–1 and 3–2, $^{13}$CO $J = 3$–2 and 6–5, and C$^{18}$O $J = 2$–1, 3–2, and 6–5. The beam size is in the lower right corner of each image. All lines of CO with the exception of the 6–5 lines are shown in log scale to amplify features. The 6–5 lines are shown on a linear scale, as they have one peak and no substructure to highlight. The contour lines shown in $^{13}$CO 3–2 and C$^{18}$O 6–5 are overlain on $^{12}$CO 2–1 to compare emission region sizes.

Cutri et al. 2003; Qi et al. 2004; Hartmann et al. 2005; Low et al. 2005; Thi et al. 2010; Andrews et al. 2012).

## 3. Modeling: RAC2D

We create a thermochemical model of the TW Hya disk that takes into account the gas and dust structure while simultaneously computing the temperature and chemical structure throughout the disk over time. Simulated observations are derived from the output model and compared to spatially resolved line observations, as well as the SED and HD line flux. We use the time-dependent thermochemical code RAC2D (Du & Bergin 2014). A brief description of the physical model follows; a higher-level detailed description of the code can be found in the aforementioned paper.

### 3.1. Physical Structure

Our model consists of three mass components: gas, a small dust ($\leqslant\mu$m) population, and a large dust ($\leqslant$mm) population. Each population is described by a global surface density distribution (Lynden-Bell & Pringle 1974), which has been widely used in modeling protoplanetary disks:

$$\Sigma(r) = \Sigma_c \left(\frac{r}{r_c}\right)^{-\gamma} \exp\left[-\left(\frac{r}{r_c}\right)^{2-\gamma}\right]. \quad (1)$$

Here $r_c$ is the characteristic radius at which the surface density is $\Sigma_c$ and $\gamma$ is the power-law index that describes the radial behavior of the surface density. Each dust population follows an MRN grain size distribution $n(a) \propto a^{-3.5}$ (Mathis et al. 1977) . The gas and small dust are spatially coupled and exist

out to 200 au (van Boekel et al. 2017; Huang et al. 2018), and they possess a scale height that is related to a critical radius (defined below). We assume that the large dust population is settled in the midplane and extends less than 100 au (Andrews et al. 2010). This reduced scale height approximates and represents the impact of dust evolution and pebble sedimentation to the midplane (Birnstiel et al. 2012; Krijt et al. 2016). The specific values for our TW Hya model are constrained by observation and detailed in the next section.

RAC2D is equipped with an exponential taper added to the surface density profile in both the inner- and outer-disk regions. This allows for more flexibility in the position of the exponential taper. If $r_c$ is defined to be larger than the gas component (which would result in a flatter disk), an exponential taper can still be added. If we were to only use Equation (1) and required a large $r_c$ value, there would be an abrupt cutoff at the user-defined outer radius. Here $r_{\rm exp}$ defines at what radius the exponential taper begins, and $r_s$ describes the strength of that taper:

$$\Sigma'(r) = \Sigma(r) e^{(r - r_{\exp_{\rm in}})/r_{s_{\rm in}}}, \text{ if } r < r_{\exp_{\rm in}}$$
$$\Sigma'(r) = \Sigma(r) e^{-(r - r_{\exp_{\rm out}})/r_{s_{\rm out}}}, \text{ if } r > r_{\exp_{\rm out}}.$$

A density profile for the gas and dust populations is derived from the surface density profile and a scale height:

$$\rho(r, z) = \frac{\Sigma(r)}{\sqrt{2\pi}\, h(r)} \exp\left[-\frac{1}{2}\left(\frac{z}{h(r)}\right)^2\right] \quad (2)$$

$$h = h_c \left(\frac{r}{r_c}\right)^{\Psi}. \quad (3)$$

Here $h_c$ is the scale height at the characteristic radius, and $\Psi$ is a power-law index that characterizes the flaring of the disk structure. The final surface densities and scale heights for each component in our model are seen in Figure 2. In the surface density plot, we show that although all of our components (gas, small dust, and large dust) have an $r_c$ value equal to 400 au, they exponentially drop off at their given $r_{\exp_{\rm out}}$.

### 3.2. Dust and Gas Temperatures

After initializing RAC2D with a model density structure for each population, the code computes a dust and gas temperature. The determination of dust and gas temperature is an iterative process, allowed to change over time owing to the evolving chemical composition. For the gas-phase chemistry, we adopt the reaction rates from the UMIST database (Woodall et al. 2007), with additional rates considering the self-shielding of CO, $H_2$, $H_2O$, and OH, as well as dust grain surface chemistry driven by temperature, UV, cosmic rays, and two-body chemical reactions on dust grain surfaces (see references given by Du & Bergin 2014). Chemical processes also provide heating or cooling to the surrounding gas. That, along with stellar and interstellar radiation, drives the thermal gas structure. Our study explores models that account for 1 Myr of chemical evolution. Although the age of TW Hya is estimated to be 5–10 Myr (Debes et al. 2013), our assumed depletion profile for CO (Section 3.3) encapsulates the effects of earlier chemical evolution of CO. We are essentially modeling the thermal physics and chemistry after that evolution has occurred. Finally, at the end of a given run we extract the dust and gas thermal profiles and SED profile.

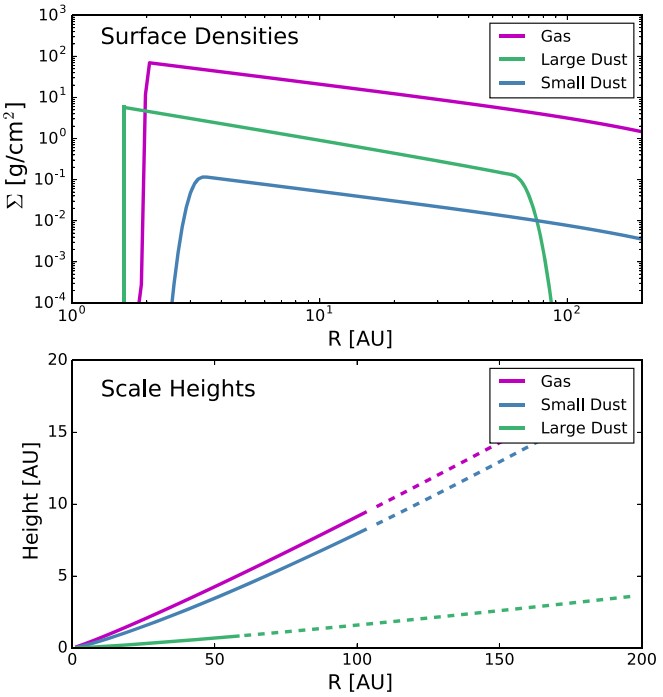


**Figure 2.** Surface density (top) and scale heights (bottom) of each component of our disk model. The exponential taper seen is added to the surface densities at 60 au for the large dust and 104 au for the small dust and gas components. The location at which the dashed line starts for the scale height also corresponds to where the exponential taper for that population begins, corresponding to a significant decrease in density.

Simulated line images for CO, $^{13}$CO, C$^{18}$O, and HD are necessary for our comparison to observations. We do not model isotopologue fractionation in this chemical network, as fractionation of CO is not significant in a massive disk like TW Hya (Miotello et al. 2014). Thus, we compute $^{13}$CO and C$^{18}$O abundances based on ISM ratios of CO/$^{13}$CO = 69 and CO/C$^{18}$O = 570 (Wilson 1999). We then apply the depletion profile to each CO line. The HD abundance (see Table 2) remains constant. Given these abundances and the local gas temperature, RAC2D computes line images using a ray-tracing technique. We then manually convolve these simulated observations with the corresponding ALMA beam to make direct comparisons to data. Our HD 1–0 observations are spatially and spectrally unresolved; thus, to re-create unresolved integrated flux measurements, we convolve our model HD line over a Gaussian corresponding to the velocity resolution of the Herschel PACS instrument: $\sim 300\,{\rm km\,s^{-1}}$ (Poglitsch et al. 2010).

The SED is created by RAC2D by counting the number of photons over a range of frequencies that interact with the disk and would fall within a given range of sight lines. Thus, photons directly emitted from the star are not accounted for, a design motivated by computational efficiency. To create the final SED, the input stellar blackbody of TW Hya (stellar mass = 0.8 $M_\odot$ and $T_{\rm eff} \approx 3400$ K) is added to the result produced by RAC2D.

### 3.3. Initial Parameter Setup of TW Hya

We set out to create a model that, given certain initial parameters and constraints for the disk physical state, produces a gas thermal profile that can reproduce the spatially resolved CO observations and other constraints. Our initial parameters

**Table 2**
Initial Chemical Abundances for Final Model

| | Abundance Relative to Total Hydrogen Nuclei |
|---|---|
| $H_2$ | $5 \times 10^{-1}$ |
| HD | $2 \times 10^{-5}$ |
| He | 0.09 |
| CO[a] | $1.04 \times 10^{-4}$ |
| N | $7.5 \times 10^{-5}$ |
| $H_2O$(ice) | $1.8 \times 10^{-4}$ |
| S | $8 \times 10^{-8}$ |
| Si+ | $8 \times 10^{-9}$ |
| Na+ | $2 \times 10^{-8}$ |
| Mg+ | $7 \times 10^{-9}$ |
| Fe+ | $3 \times 10^{-9}$ |
| P | $3 \times 10^{-9}$ |
| F | $2 \times 10^{-8}$ |
| Cl | $4 \times 10^{-9}$ |

**Note.**
[a] CO has an imposed radial depletion profile as shown in Figure 3.

are taken from Zhang et al. (2019), who compiled the most up-to-date constraints on disk parameters from the literature: Brickhouse et al. (2010), Andrews et al. (2012), van Boekel et al. (2017), Gaia Collaboration et al. (2018), and Huang et al. (2018). Source information is found in Table 3 of Zhang et al. (2019). For initial chemical abundances, we adopt values given in Table 2 motivated by Du & Bergin (2014) and Zhang et al. (2019). The disk inclination used is 6°, as past studies of TW Hya tend to use a range of inclination values between 5° and 7° (Qi et al. 2004; Andrews et al. 2012; Huang et al. 2018).

In this study, we begin with a radial CO abundance profile motivated by Zhang et al. (2019), which calculated two depletion profiles, one for $^{13}$CO and one for C$^{18}$O. They were calculated to fit the isotopologue observations. The depletion profile dictates how much CO should be depleted from the expected total value, including both gas and solid state ($\sim 10^{-4}$ for $^{12}$CO) at each radius. The difference in the observed depletion profiles between the isotopologues can be understood by differential effects between $^{13}$CO and C$^{18}$O such as fractionation and isotopic selective self-shielding (e.g., Visser et al. 2009; Woods & Willacy 2009; Miotello et al. 2014, 2016). Note that the impact of isotope selective self-shielding is much smaller than the overall removal of CO from the surface layers (Du & Bergin 2014). Hence, our initial depletion profile was the average of the $^{13}$CO and C$^{18}$O observed depletion, as shown in Figure 3. In this study, we implemented the CO depletion at the start of the chemical and thermal evolution, as the lack of CO will affect the temperature structure. We found that with the Zhang et al. (2019) CO depletion profile our simulated radial profiles did not reproduce the C$^{18}$O 2–1 and $^{13}$CO 2–1 profiles, in particular. This is due to both the chemical processing over the timescale of 1 Myr and the change in temperature at which each of these transitions emits. Reducing the chemical time to 0.01 Myr removed the effect of chemical processing, which should be encompassed through the implemented CO depletion. Further iterations on the radial CO depletion profile were made until we reached a model that reproduced the C$^{18}$O 2–1 observations within the margins of uncertainty. Our final CO depletion profile is shown in comparison to that of Zhang et al. (2019) in Figure 3. The largest difference between the two exists within the inner 20 au, where we found that we did not require as extreme a CO depletion factor. Beyond 20 au the final CO depletion profile is on average 2.5 times less than what was derived in Zhang et al. (2019).

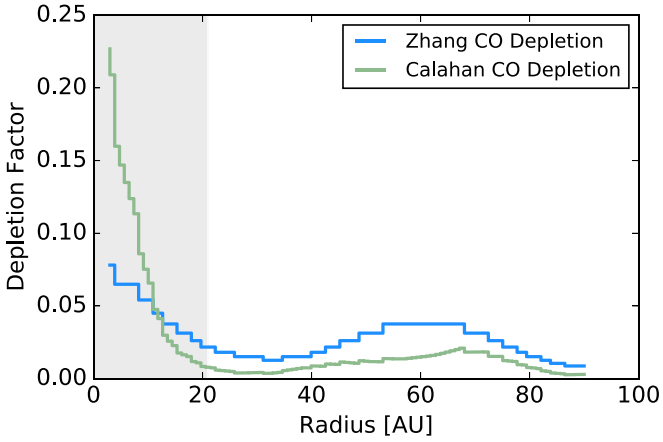


**Figure 3.** Final radial depletion profile (green) as motivated by the depletion profiles derived in Zhang et al. (2019) (blue). CO was depleted radially according to the above factor at the beginning of the thermochemical calculation. The transparent gray corresponds to the beam size of the C$^{18}$O 2–1 observation.

### 3.4. Parameter Exploration

This study relies on a suite of CO line observations, as each line provides information about a slightly different vertical layer within the disk (Gorti et al. 2011; Zhang et al. 2017; Woitke et al. 2019). As the CO observations were spatially resolved, the quality of model was assessed by a comparison of the radial integrated intensity profiles. We additionally seek to match the HD flux and the SED.

As a first step we set up a grid of models to explore the full parameter space. The parameter space and initial model parameters from Zhang et al. (2019) are shown in Table 3. Initially, we explored gas mass, small dust mass, $\Psi$, $\gamma$, and radius and height values within ranges supported by previous observation and modeling work. Each parameter is explored using values above and below the initial value. For the gas mass, our upper limit was 0.06 $M_\odot$, which is the upper limit quoted in Bergin et al. (2013), and the lower limit was 0.01 $M_\odot$, which is similar to some earlier estimates of TW Hya's gas mass (Weintraub et al. 1989b; Thi et al. 2010). The small dust mass range was motivated by the SED, limiting the range from factors of 2× greater than our initial value to ∼3× less. Both extremes produce SEDs that do not match the observations, but values in between provide a reasonable match to the SED. The $\Psi$ values explored vary from 0.8 to 1.3; both extremes affect the integrated CO emission profiles quite strongly. $\gamma$ has an upper limit of 2 (see Equation (1)); however, we explore smaller variations on gamma around an initial value of 0.85, thus using limits of 0.5–1.1. We did not explore values nearing the upper limit of 2, as past observational constraints on $\gamma$ suggest that the value for TW Hya is not much larger than 1.0 (Kama et al. 2016; van Boekel et al. 2017; Zhang et al. 2017). While this is a narrow range, it did provide enough information to understand the trends that come from changes in $\gamma$. For $r_{\exp_{out}}$, $h_c$, and $r_c$, the smallest value explored was that of the large dust value, and the largest value explored was double the initial model value. We did not explore the inner or outer edge values of $r_s$ (see Section 3.1), nor the inner exponential radial cutoff

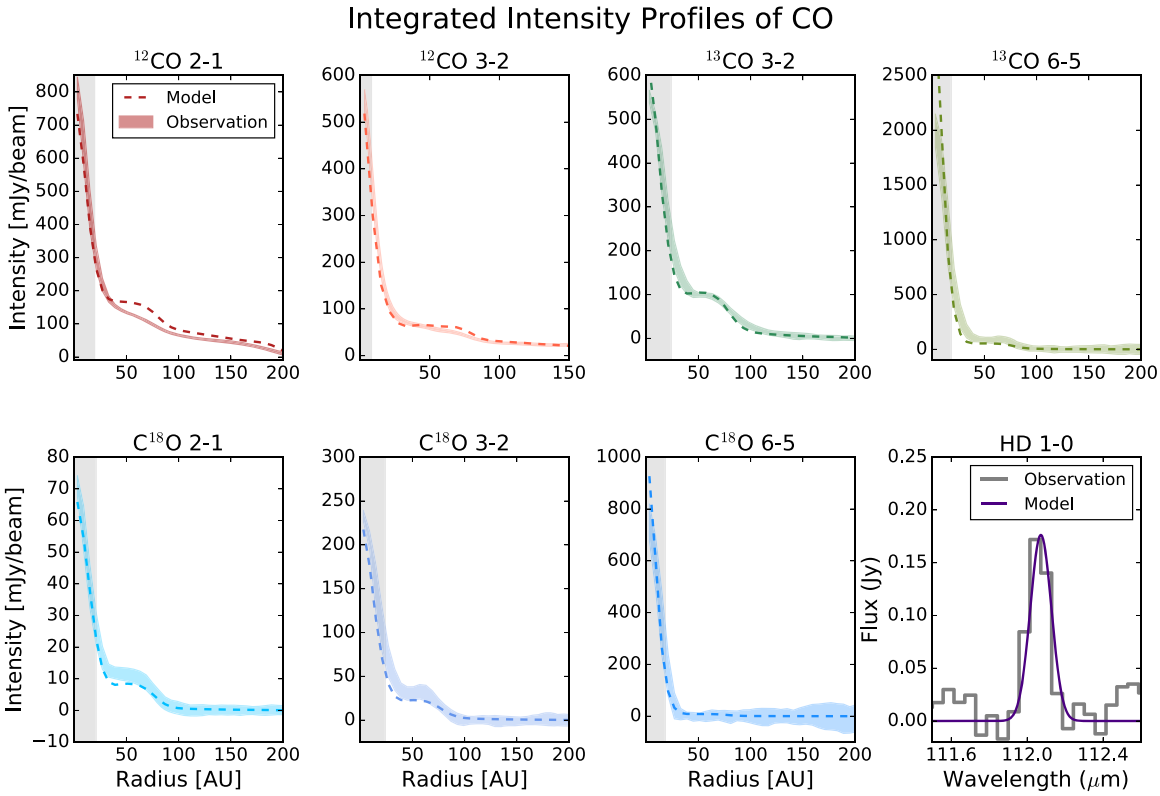


**Figure 4.** Integrated radial intensity profiles of CO and its isotopologues $^{13}$CO and C$^{18}$O. The solid lines are from observations from ALMA (see Table 1), the dashed lines are from our best-fit model, and each observation's beam is shown in the filled region. The thermal profile that produced this best match to the observation is shown in Figure 6.

**Table 3**
Gas and Dust Population Parameters: Ranges and Initial Values

| | Gas | Small Dust ($5 \times 10^{-3}$ –1 $\mu$m) | Definition |
|---|---|---|---|
| Mass ($M_\odot$) | 0.01–[0.05]–0.06 | $2.5 \times 10^{-5}$–[$1 \times 10^{-4}$]–$5 \times 10^{-4}$ | Total mass |
| $\Psi$ | 0.8–[1.2]–1.6 | 0.8–[1.2]–1.6 | Flaring parameter |
| $\gamma$ | 0.5–[.75]–1.1 | 0.5–[.75]–1.1 | Surface density power index |
| $h_c$ | 8.4–[42]–84 | 8.4–[42]–84 | Characteristic height |
| $r_{\exp_{out}}$ | 60–[104]–200 | 60–[104]–200 | Exponential drop-off radius in the outer disk |
| $r_{s_{out}}$ | 70.7 | 70.7 | Exponential drop-off strength in the outer disk |
| $r_{\exp_{in}}$ | 2 | 3.5 | Exponential drop-off radius at the inner disk |
| $r_{s_{in}}$ | 0.1 | 0.5 | Exponential drop-off strength at the inner disk |
| $r_{in}$ (au) | 0.1 | 0.5 | Inner radius cutoff |
| $r_{out}$ (au) | 200 | 200 | Outer radius cutoff |
| $r_c$ | 400 | 400 | Characteristic radius |

**Note.** This table shows the range of parameter space explored in each variable of our thermochemical model, with the initial value in brackets. Since the parameter values for the large dust do not significantly impact the thermal structure, we do not explore variations in the equivalent parameters in the large dust component and keep these fixed to the Zhang et al. values (see Table 4). All length values are in units of au.

$r_{\exp_{in}}$, as these values cannot be constrained with our CO observations. For each model we compare the model output CO isotopologue emission profiles as shown in Figure 4 in search of the best fit.

## 4. Results

### 4.1. Description of Best-fit Model

We show the results of our best-fit model in Figures 4–6. The model agrees well with all seven resolved CO lines available, along with the HD $J = 1$–0 flux and the SED profile (Figure 5). The parameter values of the best-fit model are given in Table 4.

Our beginning thermal structure was from the TW Hydra disk model of Zhang et al. (2019) (see Section 3.3). This initial model underrepresents the CO flux in the inner ~25 au while overrepresenting the CO flux between 25 and 75 au, particularly in the $^{13}$CO $J = 3$–2 and C$^{18}$O $J = 2$–1 lines (see Figure A1). The initial model HD line flux is $4.6 \times 10^{-18}$ W m$^{-2}$, which is 73% of the observed value, falling outside of the quoted error of that flux measurement from Bergin et al. (2013), $6.3(\pm 0.7) \times 10^{-18}$ W m$^{-2}$. To solve these initial discrepancies, we explore the

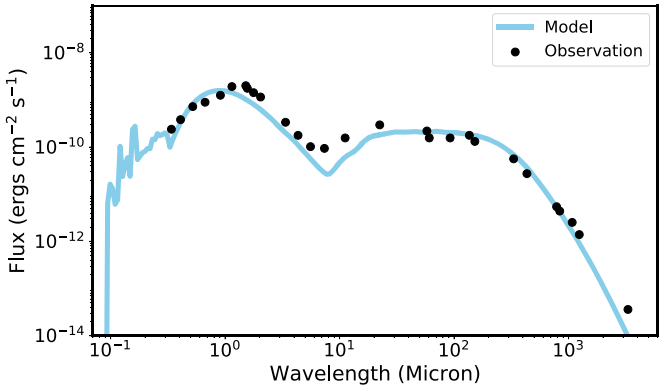


**Figure 5.** Comparison of the photometry data that composes TW Hya's SED and the modeled SED from RADMC3D based on the gaseous and dust density and temperature structures from RAC2D.

**Table 4**
Gas and Dust Population Parameters: Final Model Values

| | Gas | Small Dust ($5 \times 10^{-3}$ –1 $\mu$m) | Large Dust ($5 \times 10^{-3}$–$1 \times 10^{3}$ $\mu$m) |
|---|---|---|---|
| Mass ($M_\odot$) | 0.025 | $1.0 \times 10^{-4}$ | $4.0 \times 10^{-4}$ |
| $\Psi$ | 1.1 | 1.2 | 1.2 |
| $\gamma$ | 0.75 | 0.75 | 1.0 |
| $h_c$ | 42 | 42 | 8.4 |
| $r_{\exp_{out}}$ | 104 | 104 | 60 |
| $r_{s_{out}}$ | 70.7 | 70.7 | 10 |
| $r_{\exp_{in}}$ | 2 | 3.5 | N/A |
| $r_{s_{in}}$ | 0.1 | 0.5 | N/A |
| $r_{in}$ | 0.1 | 0.5 | 1 |
| $r_{out}$ | 200 | 200 | 200 |
| $r_c$ | 400 | 400 | 400 |

**Note.** Final values of the TW Hya model that reproduces the CO, HD, and SED observations. All length values are in units of au.

parameter space extensively (see more details in the Appendix). We find that in order to match both CO and HD observations the $\Psi$ values of the gas and small dust need to be slightly different (1.1 and 1.2, respectively). This difference creates a thin layer at the surface of the disk that is depleted of dust. The difference between the scale height of the gas and dust is 1.2% of the radial location (represented in Figure 2).

This thin layer depleted of dust is a crude way to represent the impact of coagulation and settling on the small dust population end of the assumed MRN (Dullemond & Dominik 2004). The changing values of $\Psi$ and thus scale heights can be seen as a way of representing a modified MRN distribution. Although the grain size distribution is not directly explored in this study, we find that the distribution of small grains strongly influences the final thermal structure. This relative change in scale height between dust and gas appears to be the best method to significantly increase the intensity of the CO emission in the inner 25 au. Gas in this thin upper layer is more effectively heated, as UV radiation penetrates more easily when the dust component is reduced. This heats CO gas in slightly denser regions and increases the CO emissivity.

Summing all these effects together, our best-fit model has a total gas mass that is only half of that in the Zhang et al. (2019) model. This model predicts an HD flux of $5.9 \times 10^{-18}$ W m$^{-2}$, which is well within the uncertainty of the observed flux.

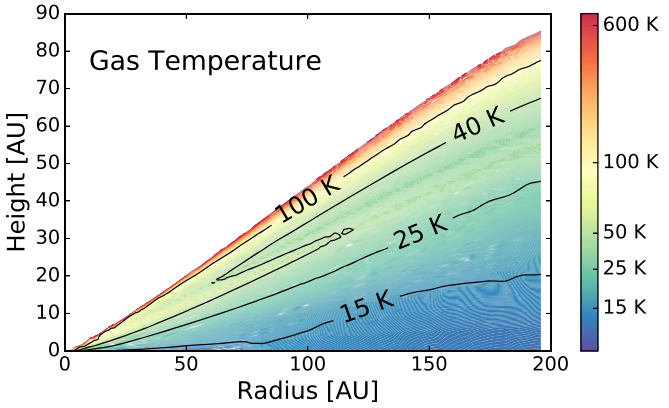


**Figure 6.** Final 2D thermal structure of the gas that reproduces seven resolved ALMA CO lines, HD flux, and the SED. The final temperature profile is supported up to scale heights from which $^{12}$CO 2–1 emits, since this transition has the highest optical depth.

(The data used to create this figure are available.)

### 4.2. Best-fit SED

The simulated SED as derived by our final TW Hya model was calculated using RADMC3D (Dullemond et al. 2012). After the temperature and physical distribution of the gas and dust were determined by RAC2D, we feed in those results including the stellar spectrum and dust opacities into RADMC3D.

Our model assumes a mass of small dust grains equal to $10^{-4}\,M_\odot$ and a mass of the large dust grains to be $4 \times 10^{-4}\,M_\odot$. Using these dust components, our model SED agrees reasonably well with the observed SED; see Figure 5. TW Hydra also exhibits a strong silicate feature near 10 $\mu$m, which our dust model underpredicts. Previous studies have successfully modeled this feature by utilizing a special type of silicate within 4 au (Calvet et al. 2002; Zhang et al. 2013). This is a scale much smaller than we aim to constrain, and it is a small effect in comparison to the total dust opacity in this region. The SED beyond $\sim$8 $\mu$m tests whether we are correctly representing the dust population, as the long-wavelength portion of the SED is mostly affected by dust mass, size distribution, spatial distribution, and composition (a mixture of silicates and graphite). Overall, our dust model provides a good match to the observed SED. Since the small dust population has an effect on the thermal balance, the SED provides one of the key factors to constrain the HD emission and overall disk mass.

### 4.3. $^{13}C^{18}O$ Flux

Using our final model, we seek to compare the observed $^{13}$C$^{18}$O flux toward TW Hya as presented in Zhang et al. (2017). We use line information for $^{13}$C$^{18}$O derived by HITRAN (Rothman et al. 2005), formatted to be identical to line data from the Leiden Atomic and Molecular Database. We also use an abundance ratio $^{12}$CO/$^{13}$CO = 40, as measured by Zhang et al. (2017) for this specific observation.[20] The resultant flux is shown in Figure A14. Overall, our model provides a good fit to the observations, underpredicting the $^{13}$C$^{18}$O flux by at most 12 mJy km s$^{-1}$ beam$^{-1}$, or about a factor of two across

[20] We note that this is different from the assumed isotope ratio for the surface layers. However, it is a direct measurement and is suggested by Zhang et al. (2017) to be the result of carbon fractionation in the dense colder layers of the photodissociation region (see discussion and results in Röllig & Ossenkopf 2013).

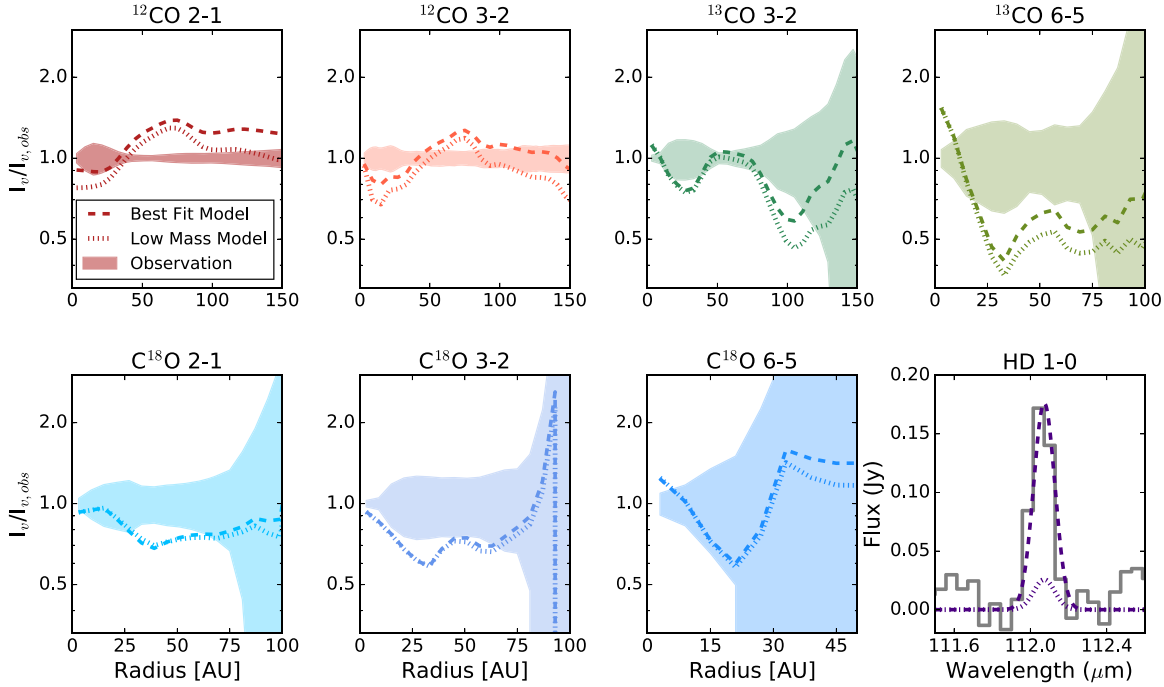


**Figure 7.** Radial intensity profiles of the observations, best-fit model, and low-mass model all normalized to the observations, along with the HD flux observations compared to the simulated HD flux in the low-mass model. The observations are thus centered around 1 and the observed error of the integrated intensity line profile defines the width of the shaded region over radius. The thick dashed line represent the best fit model (see Figure 4), and the thin dashed line represents the low-mass model (with high CO abundance). From this comparison, we can see that the models with gas masses of 0.025 and 0.0025 $M_{\odot}$ have nearly identical profiles. This also shows how close our model represents the observations. The majority of the time, the modeled flux is within a factor of two of the observed, with the only exceptions being when the observations drop quickly to receive zero flux and the model does not reach zero as quickly; however, the model still is within the error. This happens especially with $C^{18}O$ 6–5. While in the low-mass model the CO remains relatively similar, the HD flux drops significantly.

the modeled flux-emitting area. As the $^{13}C^{18}O$ emission is highly centrally concentrated, the location of largest discrepancy is in the central regions and also toward the observed asymmetry. This residual value is similar to the background noise flux. The asymmetry can be accounted for by simply the low signal-to-noise ratio for this observation.

### 4.4. CO Mass/Abundance Degeneracy

Our exploration of the parameter space shows that the CO line intensity is a degenerate result of the total gas mass and CO abundance. If the line is optically thin, the CO emission scales directly with its number density, $n_{CO}$, where $n_{CO}$ is $x_{CO} \times n_{H_2}$. Even in the case of optically thick lines, as the gas density increases, CO emission becomes optically thick at a higher location of the disk atmosphere; thereby tracing temperature of a warmer region. Thus, there is a degeneracy between the abundance of CO and the density of $H_2$ and hence the gas mass. One way to break this degeneracy is with an observed HD flux, as it is independent of CO abundance.

To explore this, we create a low-mass model based on the parameters of our best-fit model; however, in this model we decrease the total gas mass by one order of magnitude while subsequently increasing in the CO abundance by the same factor. As shown in Figure 7, this low-mass model produces indistinguishable CO radial profiles compared to those of our best-fit model. However, the line flux of the HD (1–0) transition of the lower-mass model goes down by more than a factor of five (see bottom right panel in Figure 7). This degeneracy between CO abundance and gas mass has been reported in previous

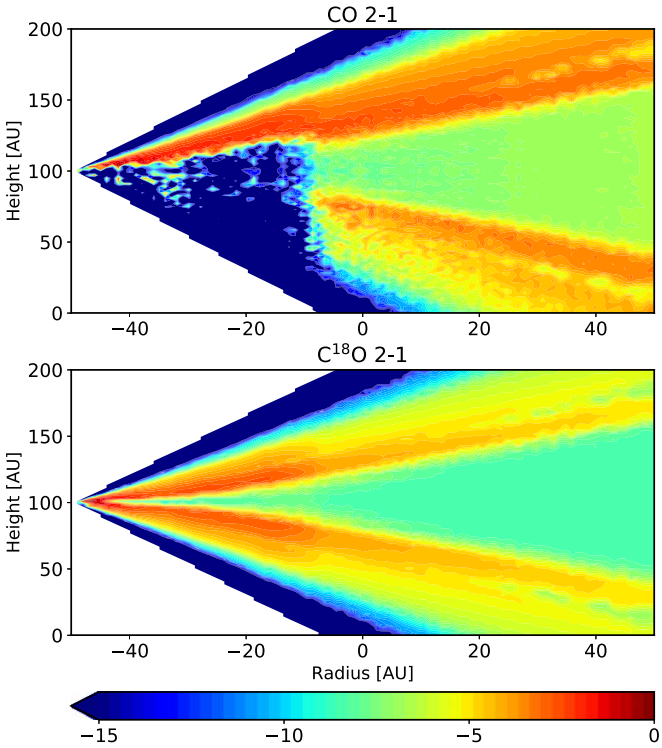


**Figure 8.** Emitting regions of $^{12}CO$ and $C^{18}O$ 2–1 in our final model. Emitting regions for each molecule were calculated based on the final model and were used to create Figure 9, which encapsulates the regions in which most of each molecule is emitting from.

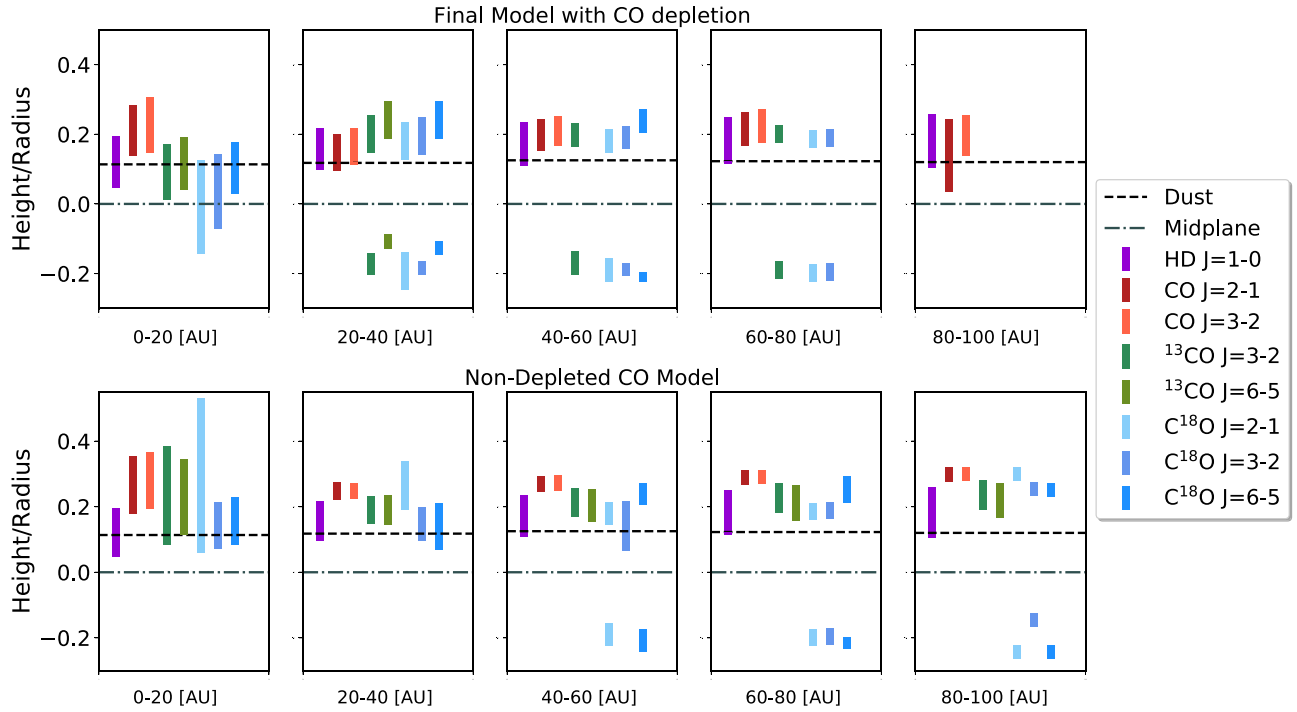


**Figure 9.** Average vertical emitting region of each line used in this study for our final model (top) and a version of that model without assuming CO depletion (bottom). For every 20 au the average vertical emitting height was calculated. The top of each bar corresponds to the average surface that consists of 90% of the flux. The bottom of the bar and below is 10% of the total flux. Lines that have two emitting regions, one above the disk and one below, are optically thin; thus, observations of these molecules come from both the front and back of the disk. There is no emission in the midplane outside the CO snowline; thus, for an optically thin emitter, their emitting regions were calculated twice: once for above the midplane, and then again but only from the back. The continuous $\tau = 1$ surface of the dust at the frequency of HD $J = 1$–0 is shown via the dashed line. Examples of 2D contribution plots used to create this figure of $^{12}$CO 2–1 and C$^{18}$O 2–1 are shown in Figure 8.

studies with less well-constrained temperature structures (Bergin et al. 2013; Favre et al. 2013; Kama et al. 2016; McClure et al. 2016; Trapman et al. 2017). Here we prove that the degeneracy cannot be broken even when the thermal structure of the disk is well constrained. In short, CO lines alone are not sufficient to constrain the total disk mass, and another independent mass tracer must be introduced, such as HD.

## 5. Analysis and Discussion

### 5.1. CO-emitting Regions

RAC2D calculates the emitting regions for each isotopologue; examples of $^{12}$CO 2–1 and C$^{18}$O 2–1 are shown in Figure 8. To allow for intermolecular comparison, we then calculated the heights at which the majority of the emission originates. This is presented in Figure 9, where we show a visualization of the average vertical cross section of the disk from which each line is emitting based on our final model. For comparison, a non-CO-depleted model is also shown. A dashed line representing the $\tau = 1$ surface of the small dust at the frequency of the HD $J = 1$–0 transition ($\lambda \simeq 112\ \mu$m) is plotted as a reference. These two models represent two extremes of T Tauri disks, a high CO abundance (which corresponds to a CO/H$_2$ ratio equal to that of the ISM) and a low CO abundance, using the relatively high CO depletion factors found in TW Hya.

In the nondepleted case, $^{12}$CO emits from a higher layer than all other isotopologues, while HD and $^{13}$CO, and in some cases C$^{18}$O, probe similar depths. C$^{18}$O appears to be optically thin, especially past 60 au; the C$^{18}$O surface brightness is therefore not a sufficient temperature tracer across a disk with similar properties to TW Hya. In this instance C$^{18}$O probes the total column density. TW Hya is, however, thought to exhibit severe CO depletions; thus, CO and its isotopologue emission will have reduced optical depth (in comparison to the nondepleted model). In our final model, $^{12}$CO 2–1 and 3–2 and $^{13}$CO 3–2 emit from roughly an equivalent vertical depth as HD, showing that in this disk observations of $^{12}$CO 2–1 and 3–2 and $^{13}$CO 3–2 best trace the layers where HD emission arises. Within radii ranging from 0 to 40 au, $^{13}$CO 3–2 emission is optically thick, overlapping with the lower bound of the HD emitting layer. The C$^{18}$O and $^{13}$CO 6–5 become optically thin beyond radii of 20–40 au; thus, their brightness temperature no longer constrains the disk surface temperature. Based on this result, the disk mass for TW Hya could have been accomplished using only the resolved observations of $^{12}$CO 2–1 and 3–2 and supplemented with $^{13}$CO 3–2 alongside HD. For future observations, multiple observations of CO are still required, at least down to the 3–2 levels, as CO depletion and gas mass are not known a priori.

### 5.2. Scattered-light Effects

TW Hya has been observed in scattered light, which traces out the small dust population of the disk. These observations are reported in van Boekel et al. (2017), and using the scattered-light observations, they find that radial depressions in the small dust surface density are necessary to reproduce the observed surface brightness. The two largest depressions in the surface density have depths of 80% and 45% at approximately 5 and 90 au, respectively (see Figure 11 in van Boekel et al. 2017). We applied this depletion factor to the small dust population to the initial model and found that it did not strongly effect the radial profiles as shown in Figure 10. The depletion does increase the HD $J = 1$–0 flux by 30%. However, the effect on $^{12}$CO and C$^{18}$O is much less (below 15%), and these

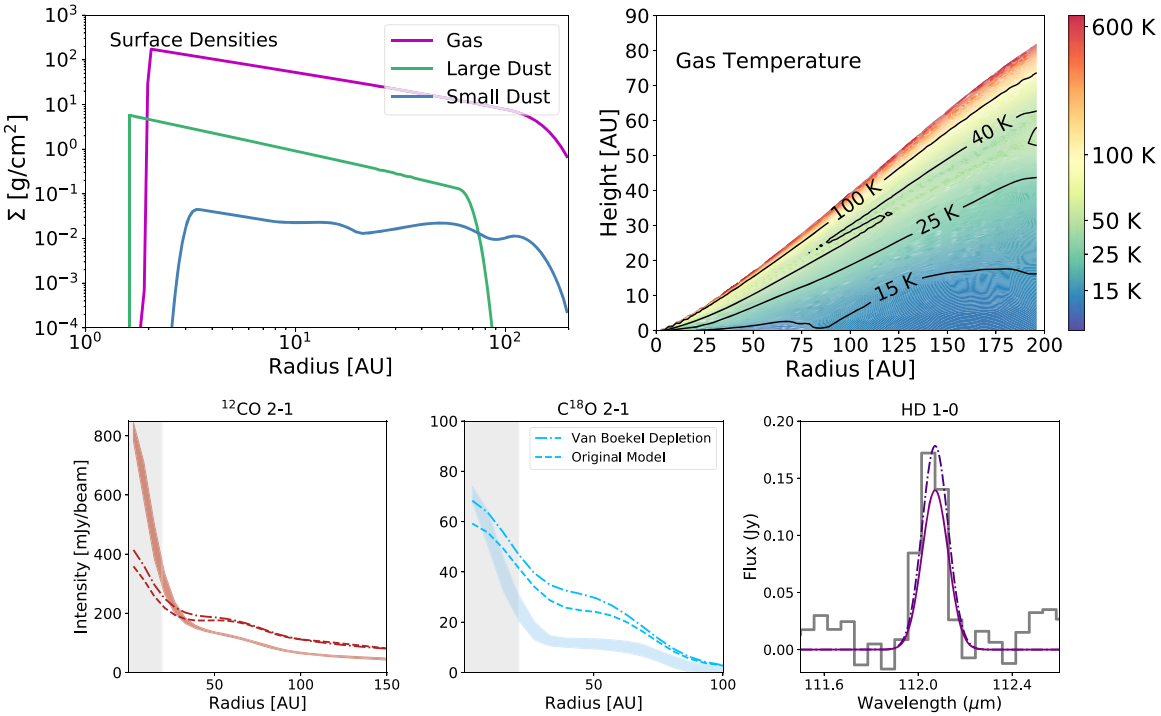


**Figure 10.** Top left: surface densities for the gas and dust populations while taking a depletion of small dust as measured by van Boekel et al. (2017) from scattered-light observations. Using the new small dust population, we calculate the gas temperature (top right), the radial profiles of $^{12}$CO and C$^{18}$O 2–1 (bottom left and bottom middle), and HD flux (bottom right). The dashed lines in the radial profile and HD flux plot show our initial model, compared to a model with a nonsmooth small dust surface density as motivated by the scattered-light observations.

changes do not significantly alter the fit to the CO radial profiles. Future modeling efforts may want to include information from the millimeter-continuum and scattered-light observations as an additional constraint on the physical state of surface layers.

### 5.3. Comparison to Other Models

There are at least two other attempts to model TW Hydra with thermochemical codes: Kama et al. (2016) with the DALI 2D physical-chemical code, and Woitke et al. (2019) with the ProDiMo code.

Kama et al. (2016) focused on tracing volatile carbon in TW Hya. To do so, they modeled an underlying thermal structure of both the gas and dust population using DALI (Bruderer et al. 2009, 2012; Bruderer 2013), which is designed and operated in a very similar way to RAC2D. This study utilized spatially unresolved observations of the CO ladder (upper limits of $J = 36$–35, 33–32, 29–28, and line fluxes of $J = 18$–17, 10–9, 6–5, ALMA observation of $J = 3$–2, and SMA observation of $J = 2$–1). Their observation of CO $J$ 3–2 was spatially resolved. Additionally, they utilized other carbon carrier molecules (C[I], C[II], $C_2H$, $HCO^+$) to motivate their models along with HD $J = 1$–0 and $J = 2$–1. Kama et al. (2016) produced a model that reproduces their CO observations and the HD flux. DALI has since been updated to include deuterium chemistry and isotopologue selective chemistry following work by Miotello et al. (2014). This subsequent updated model is presented in Trapman et al. (2017) and shown in Figure 11, alongside our RAC2D results. The main difference between the Kama et al. (2016) model and ours is that we reproduce multiple spatially resolved CO transitions. Our ∼15–100 K isotherms match up relatively well, which are the temperature ranges that our CO lines trace. Our solutions do diverge from each other at high temperatures (>100 K). Using the HD emission, Kama et al. (2016) derived gas mass and determined the same value that this study independently arrived at: 0.023 $M_\odot$.

Woitke et al. (2019) describes the DIANA project, which modeled a number of protoplanetary disks in a homogeneous way using SED matching and the thermochemical code ProDiMo. Their model outputs for each disk are publicly available. Figure 11 shows a comparison of their results with our RAC2D model. The most noticeable difference is that our model appears to have a higher gas scale height compared to that determined by the DIANA project. Further, the DIANA model finds higher gas temperatures at the disk surface, along with a comparatively cooler midplane (e.g., compare 15 K isotherms). Woitke et al. (2019) matched many volatile lines such as CO and $H_2O$ to within a factor of two. However, they underpredicted the HD emission by a factor of 13 with a total gas mass of 0.045 $M_\odot$.

Cleeves et al. (2015) also produced a TW Hya model with the primary goal of fitting molecular ion observations. In the process, this paper used SMA observations of C$^{18}$O and $^{13}$CO $J = 2$–1 and the Herschel HD observation to constrain the physical structure. The chemical model employed was not a self-consistent thermochemical model; however, the gas temperature structure was derived via a DALI-based fitting function to account for the gas and dust thermal decoupling in the upper layers. In the Cleeves et al. (2015) model, the derived gas mass of $0.04 \pm 0.02\ M_\odot$ is also in good agreement with our best-fit model, as is the overall temperature profile.

### 5.4. Future Observations of Spatially Resolved CO Line Emission in Inclined Disks

This study serves as a proof of concept that observation and subsequent modeling of resolved CO lines and HD line flux in

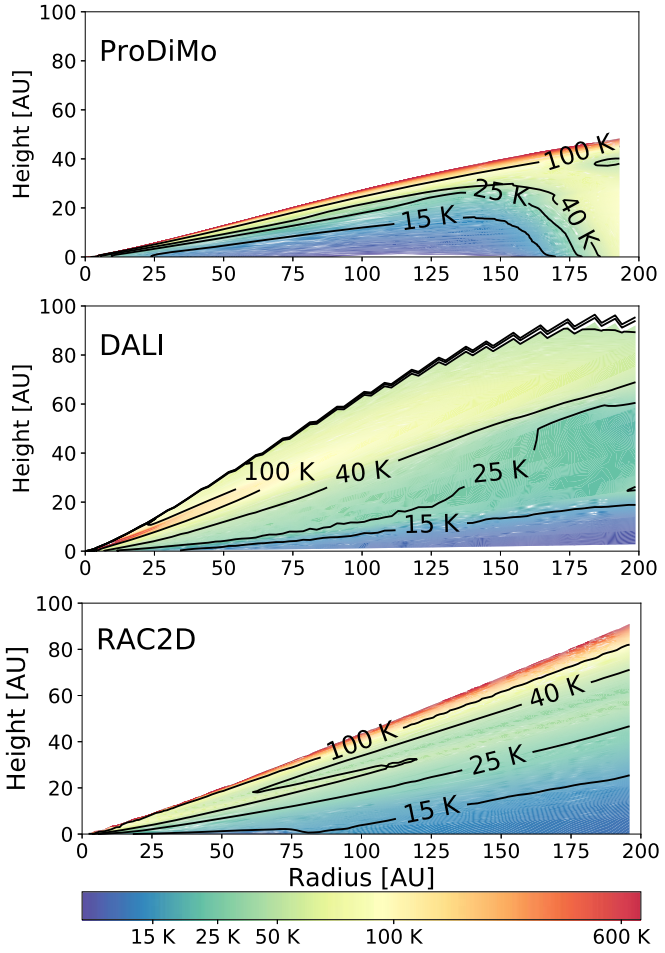


**Figure 11.** Comparison of the gas thermal structure of TW Hya from Woitke et al. (2019), Kama et al. (2016), and this study.

combination with the SED are a powerful method to uncover thermal structure and disk mass. TW Hya is an ideal disk to test out this new method, as it is has been extensively observed with ALMA and other observatories and is one of only three disks with an HD emission detection (McClure et al. 2016). One disk parameter not explored in this particular study is disk inclination. An inclined disk will allow for direct constraints to be set on the vertical emitting layer and the subsequent temperature inferred within the layer (Pinte et al. 2018; Teague et al. 2019). Disk inclination will broaden the spectral line, and the degree at which that might complicate extraction of a 2D thermal structure using thermochemical models is worth investigation. It is also worth applying these techniques toward brighter Herbig Ae/Be disks. The CO snowline in these systems lies at greater distances from the star (Qi et al. 2015; Zhang et al. 2020a), and hence some transitions might probe layers closer to the midplane than sampled in T Tauri systems.

In our model we do not take CO fractionation chemistry into account. However, this would not effect the derived temperature structure very strongly. $^{12}$CO would be unaffected, and selective photodissociation has a marginal effect for $^{13}$CO. There would be a larger effect for C$^{18}$O; however, its emission is optically thin for much of the disk and thus does not provide sufficient temperature information. We also did not include rarer isotopologues of CO such as $^{13}$C$^{18}$O (Zhang et al. 2017), which would provide additional insight into column density inside the CO snowline.

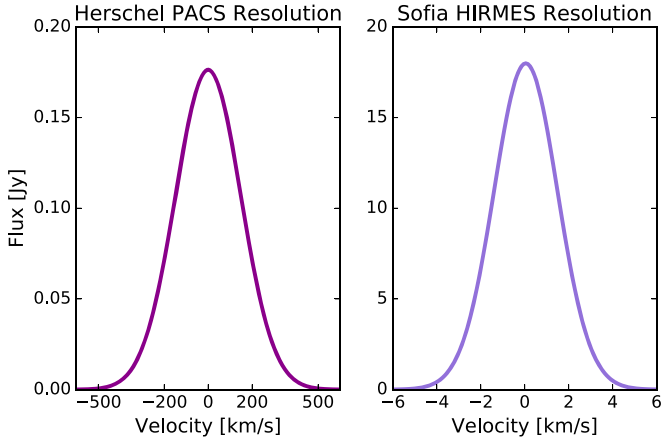


**Figure 12.** Predicted HD spectra based on the resolution of the proposed HIRMES instrument on SOFIA (right) compared to the modeled spectra of HD $J = 1$–0 from this study using the spectral resolution of the PACS instrument.

### 5.5. Future HD Observations

At present, the sample of disks in which HD has been targeted is limited to a few deep observations (McClure et al. 2016) and those with full Herschel PACS scans, such as the upper limits on HD emission in Herbig disks by Kama et al. (2020). More observations are necessary to further our understanding of protoplanetary disks. There are future instruments and observatories potentially on the horizon that will observe the frequency range in which HD resides, and with a much higher resolution and sensitivity than Herschel. These observatories will have the ability to drastically improve our understanding of early planet formation environments. The HIRMES instrument was proposed to be added to the SOFIA observatory, offering a spectral resolution of 3 km s$^{-1}$ at 112 $\mu$m. If built and deployed, HIRMES was projected to have a sensitivity similar to PACS (Richards et al. 2018) and could perform deep surveys for HD emission, opening up the ability to provide a robust diagnostic of gas mass. The planned spectral resolution on HIRMES is enough to fully resolve the HD emission line for inclined disks, which will provide unique constraints on the radial distribution of disk gas. A simulated HIRMES observation of TW Hya based on this model is shown in Figure 12.

Looking onward, National Aeronautics and Space Administration's (NASA) Origins Space Telescope, if funded and launched, provides a sensitivity improvement at 112 $\mu$m of over three orders of magnitude compared to Herschel, enabling deep surveys of over 1000 disks. Origins could provide sensitivities toward the HD line corresponding to gas disk masses down to $10^{-5}\,M_{\odot}$ (Trapman et al. 2017). These future or potential observatories in combination with future resolved suites of CO lines via ALMA will be incredibly insightful toward our understanding of planet formation, enabling the ability to track the 2D temperature structure and the gas mass, thereby revealing the key physical conditions under which planets form.

## 6. Conclusions

Using the thermochemical code RAC2D; observations from the TW Hya Rosetta Project taken with ALMA of $^{12}$CO $J = 2$–1 and C$^{18}$O $J = 2$–1; archival ALMA data of $^{12}$CO 3–2, C$^{18}$O 3–2 and 6–5, $^{13}$CO 3–2 and 6–5, and HD $J$ 1–0; and the system's SED, we find the following:

1. We derive a thermal structure of the TW Hya disk that fits radial brightness profiles of seven spatially resolved CO line transitions, a spatially unresolved HD line flux, and the SED. This study is the first to reproduce multiple spatially resolved observations of CO using a thermochemical model. We compare our results to thermal structures derived by other methods.
2. Using the derived thermal structure and the HD (1–0) line flux, we constrain the total gas mass of the TW Hya disk to be $\approx 0.025\ M_{\odot}$ within our model framework.
3. We directly demonstrate that CO line brightness distributions are degenerate results of the CO abundance and the total gas mass of the disk. Therefore, CO alone cannot be used as a robust tracer of the total gas mass, for any protoplanetary disk system. We find that using observations of HD is one solution that breaks this degeneracy.

This paper makes use of data from ALMA programs 2015.1.00686.S, 2016.1.00629.S, 2012.1.00422.s, and 2016.1.00311.S. ALMA is a partnership of ESO (representing its member states), NSF (USA), and NINS (Japan), together with NRC (Canada) and NSC and ASIAA (Taiwan), in cooperation with the Republic of Chile. The Joint ALMA Observatory is operated by ESO, AUI/NRAO, and NAOJ. The National Radio Astronomy Observatory is a facility of the National Science Foundation operated under cooperative agreement by Associated Universities, Inc. J.K.C. acknowledges support from the National Science Foundation Graduate Research Fellowship under grant No. DGE 1256260 and the National Aeronautics and Space Administration FINESST grant, under grant No. 80NSSC19K1534. E.A.B. acknowledges support from NSF grant No. 1907653. K.Z. acknowledges the support of the Office of the Vice Chancellor for Research and Graduate Education at the University of Wisconsin – Madison with funding from the Wisconsin Alumni Research Foundation, and support of the support of NASA through Hubble Fellowship grant HST-HF2-51401.001. awarded by the Space Telescope Science Institute, which is operated by the Association of Universities for Research in Astronomy, Inc., for NASA, under contract NAS5-26555. L.I.C. gratefully acknowledges support from the David and Lucile Packard Foundation and the Virginia Space Grant Consortium. S. A. and J. H. acknowledge funding support from the National Aeronautics and Space Administration under Grant No. 17-XRP17 2-0012 issued through the Exoplanets Research Program. J. H. acknowledges support for this work provided by NASA through the NASA Hubble Fellowship grant \#HST-HF2-51460.001-A awarded by the Space Telescope Science Institute, which is operated by the Association of Universities for Research in Astronomy, Inc., for NASA, under contract NAS5-26555. C.W. acknowledges financial support from the University of Leeds and the Science and Technology Facilities Council (STFC; grant No. ST/R000549/1). M.K. gratefully acknowledges funding by the University of Tartu ASTRA project 2014-2020.4.01.16-0029 KOMEET "Benefits for Estonian Society from Space Research and Application," financed by the EU European Regional Development Fund. K.Ö. acknowledges support from the Simons Foundation (SCOL 321183) and an NSF AAG Grant (#1907653).

*Facilities:* ALMA, Herschel.

*Software:* RAC2D (Du & Bergin 2014), bettermoments (Teague & Foreman-Mackey 2018), CASA (McMullin et al. 2007).

## Appendix
## Parameter Effects on Simulated Observations

Through exploration of our model and the parameter space of the properties listed in Table 3, we find that CO emission is most strongly affected by gas and small dust parameters. Here we list how the CO integrated intensity profiles respond to changes in parameters. These findings are specific to this TW Hya model but can be extrapolated to similarly inclined gaseous disks. The following discussion is based on the model parameter values from Zhang et al. (2019) presented in Figure A1.

### *A.1. $\gamma$: Power-law Index of Surface Density*

$\gamma$ is a power-law index for the surface density (see Equation (1)) with a maximum value of 2. Increasing $\gamma$ affects the distribution by concentrating the given component (gas, dust) toward the inner disk region, increasing the column density of gas and dust. A decrease in $\gamma$ results in a more even distribution of the mass component. It has the strongest effect on the emission arising from the inner 25 au, especially for the rare isotopologues (see Figures A2 and A3). Altering gamma from 0.75 to 0.9 in both small dust and gas results in very little change in $^{12}$CO 2–1 and 3–2, but at least a 10% increase across all C$^{18}$O lines. In our final model, we increased $\gamma$ in both the gas and small dust, as they are coupled, from 0.75 to 0.85, which aided in adding to the intensity in the inner 25 au.

### *A.2. $\Psi$: Power-law Index for Scale Height*

Typical $\Psi$ values are between 1.1 and 1.2 for TW Hya and affect the scale height over different radii, with an increase in the flaring as $\Psi$ increases. Changes in $\Psi$ down to 0.05 have a significant effect on the final integrated intensity profiles. Generally, lowering $\Psi$ results in an increase in intensity in the inner disk (<25 au), and beyond ≈25 au features are "smoothed" out (see Figures A4 and A5). This is due to the increase of gas surface density toward the inner au when flaring decreases. The most extreme value of $\Psi$ we explored was 1.6, and at that point the modeled intensity profiles plummeted down to 25% or less of their original flux within 20 au. Beyond 20 au, there is emission comparable to the original model. The thermal profile derived from the initial parameters (shown in Table 3 and discussed in Section 3.3) produced CO lines that were too dim within 25 au by a factor of 2 in $^{12}$CO, $^{13}$CO 6–5, and C$^{18}$O 6–5 and ∼30% in $^{13}$CO and C$^{18}$O 3–2. We find that the only way to significantly brighten the inner regions while simultaneously keeping the intensity in the outer regions low is to allow the gas and small dust to have slightly different $\Psi$ values. The gas component is given a $\Psi$ value of 1.1, while the small dust is given $\Psi = 1.2$. Due to the fact that our critical radius is beyond the gaseous radius, even though the dust has a higher flaring angle, it lies below the gas. This creates a thin region at the upper layer of the disk where only gas resides; this region has a thickness of ∼1.2% of a given radius. In this gas-rich layer, CO and HD lines become brighter, noticeably within the inner few au. There are no other parameters that we explored that accomplished this, the closest being $\gamma$, which increases emission within 50 au but smooths out the feature beyond 50 au.

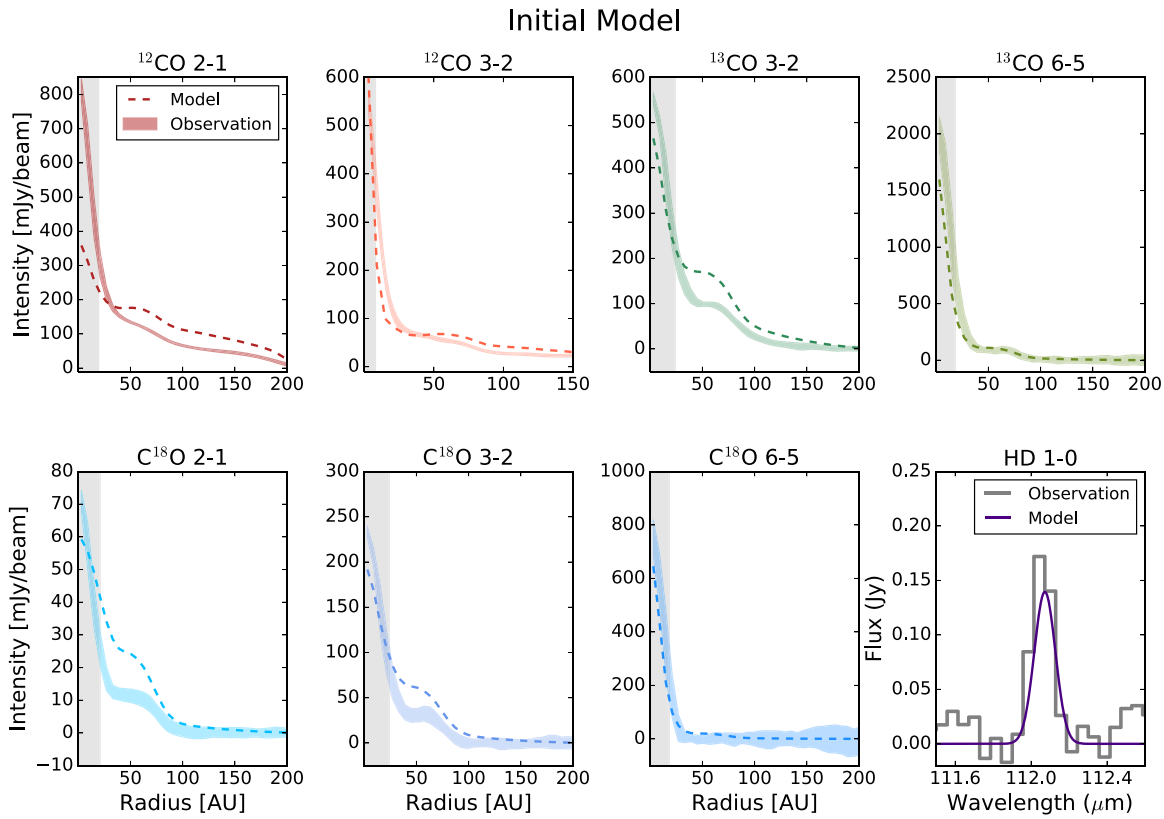


**Figure A1.** Integrated line profiles of CO and its isotopologues from ALMA observations (solid lines) and the simulated observations from RAC2D using model parameters from Zhang et al. (2019) and listed in Table 3.

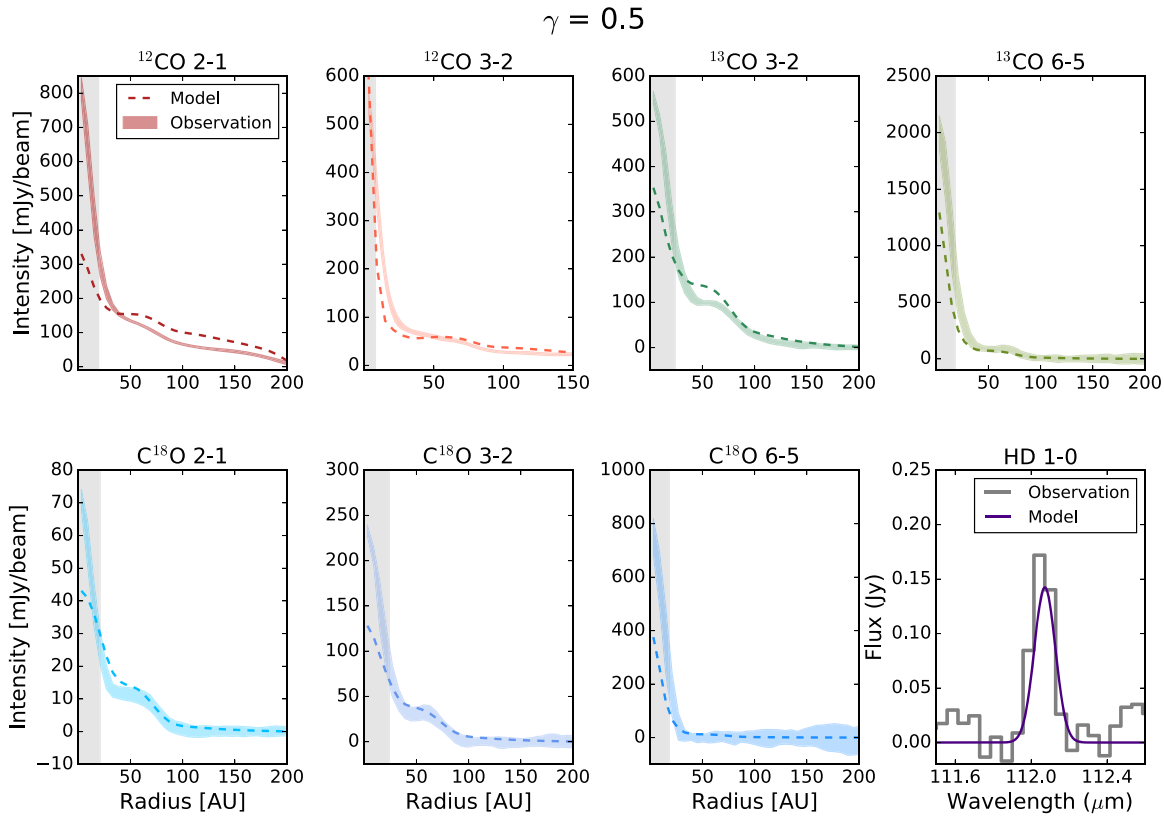


**Figure A2.** Integrated intensity profiles of observations and a model based on the initial model (Figure A1) but with $\gamma$ in the gas and small dust = 0.5.

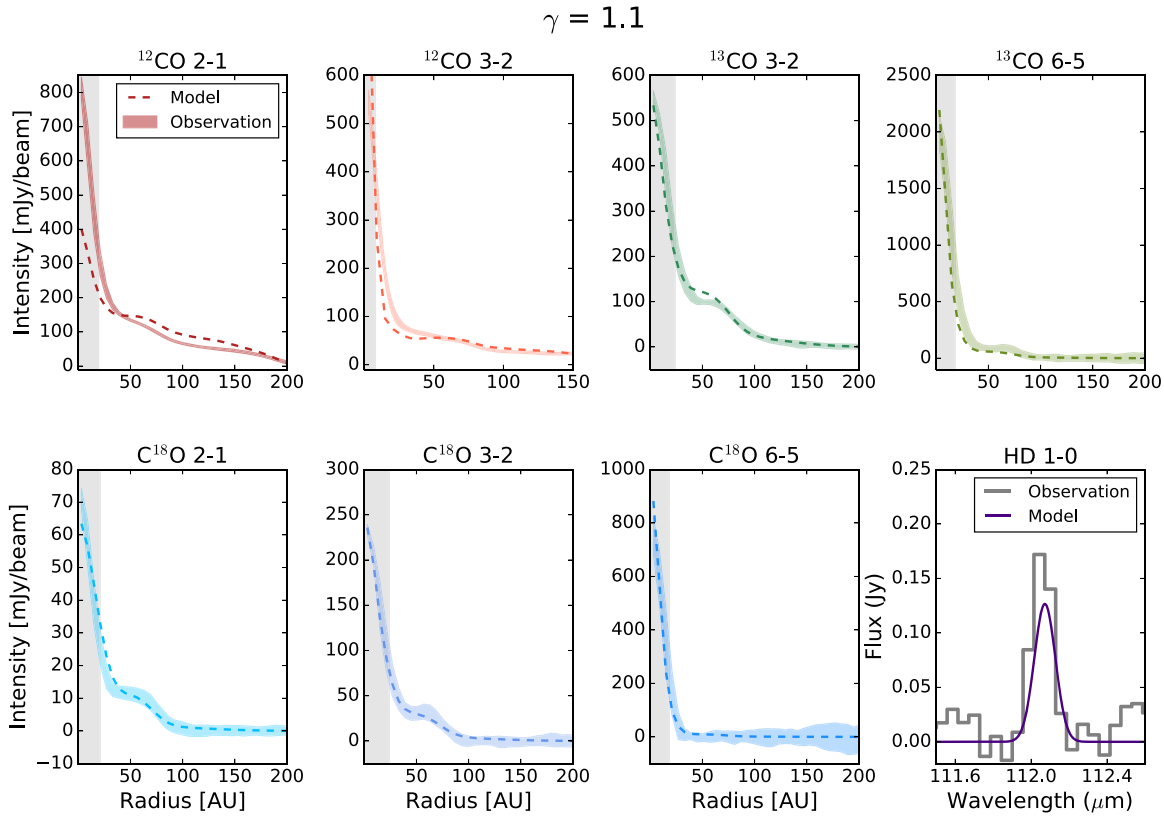


**Figure A3.** Integrated intensity profiles of observations and a model based on the initial model (Figure A1) but with $\gamma$ in the gas and small dust = 1.1.

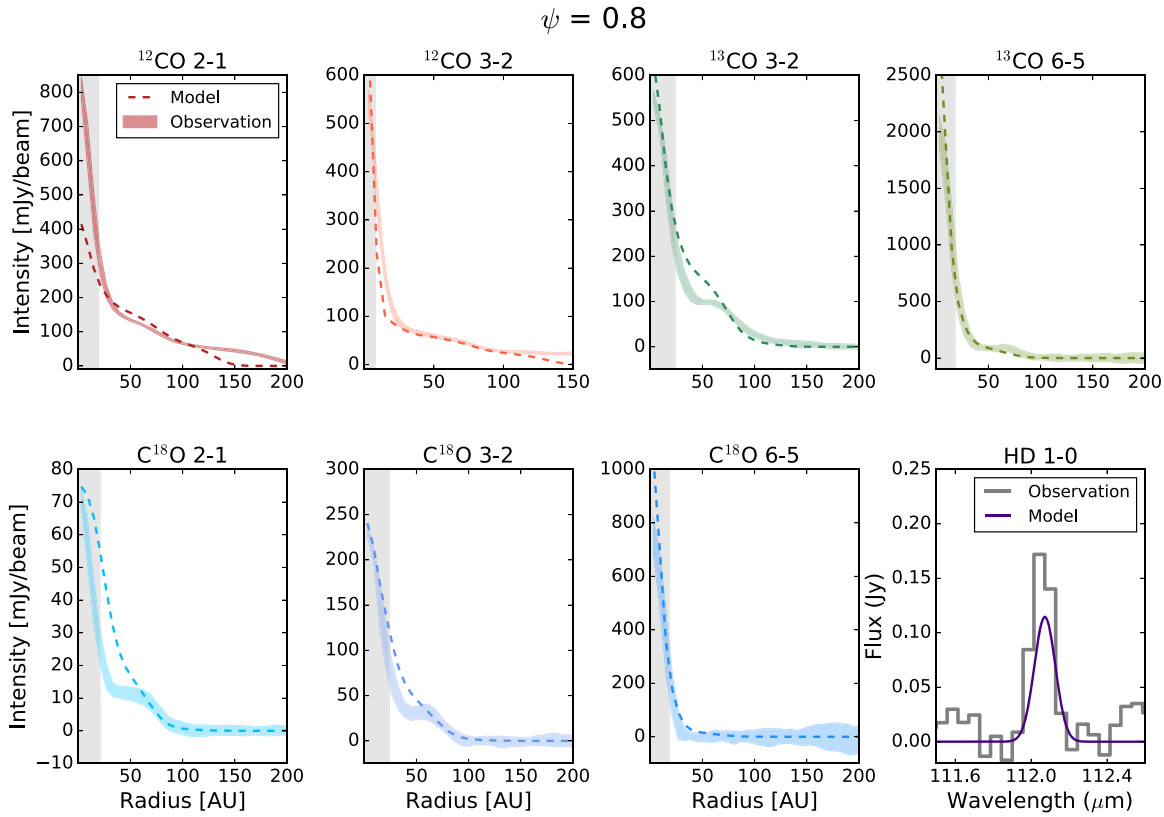


**Figure A4.** Integrated intensity profiles of observations and a model based on the initial model (A1) but with $\Psi$ in the gas and small dust = 0.4.

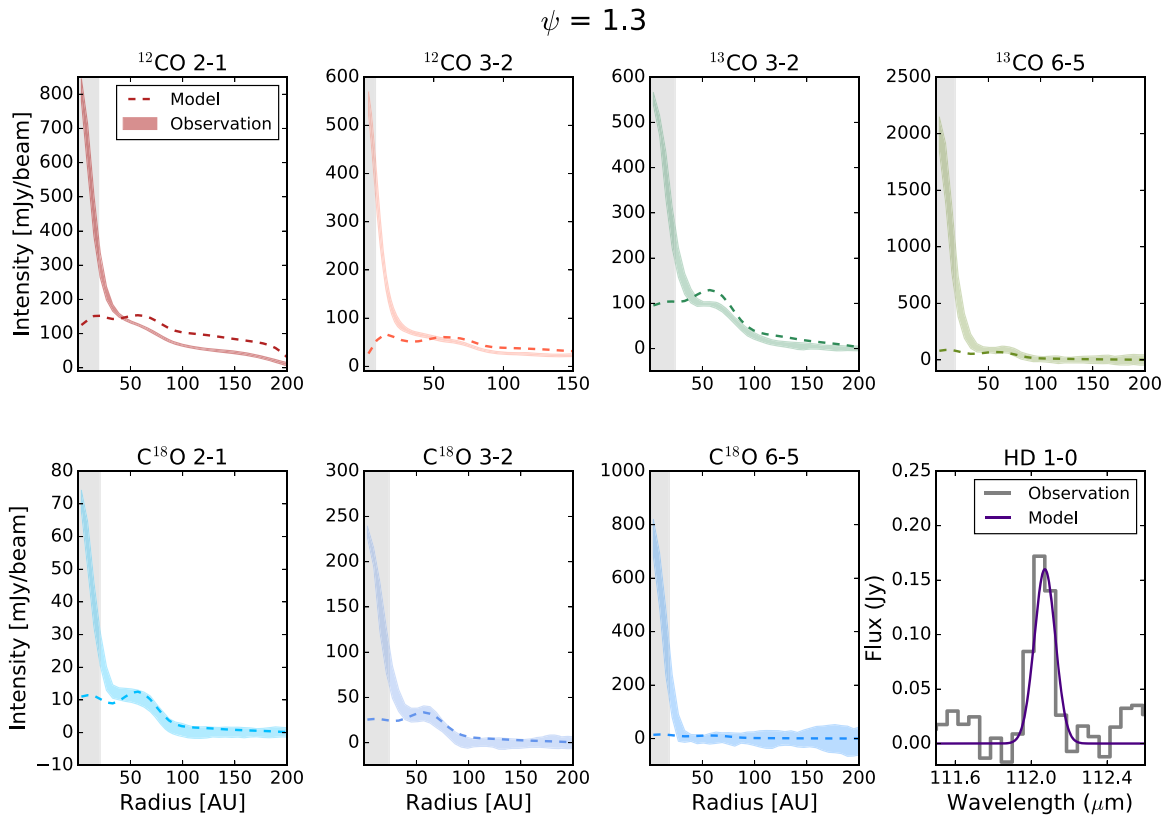


**Figure A5.** Integrated intensity profiles of observations and a model based on the initial model (Figure A1) but with $\Psi$ in the gas and small dust = 1.6.

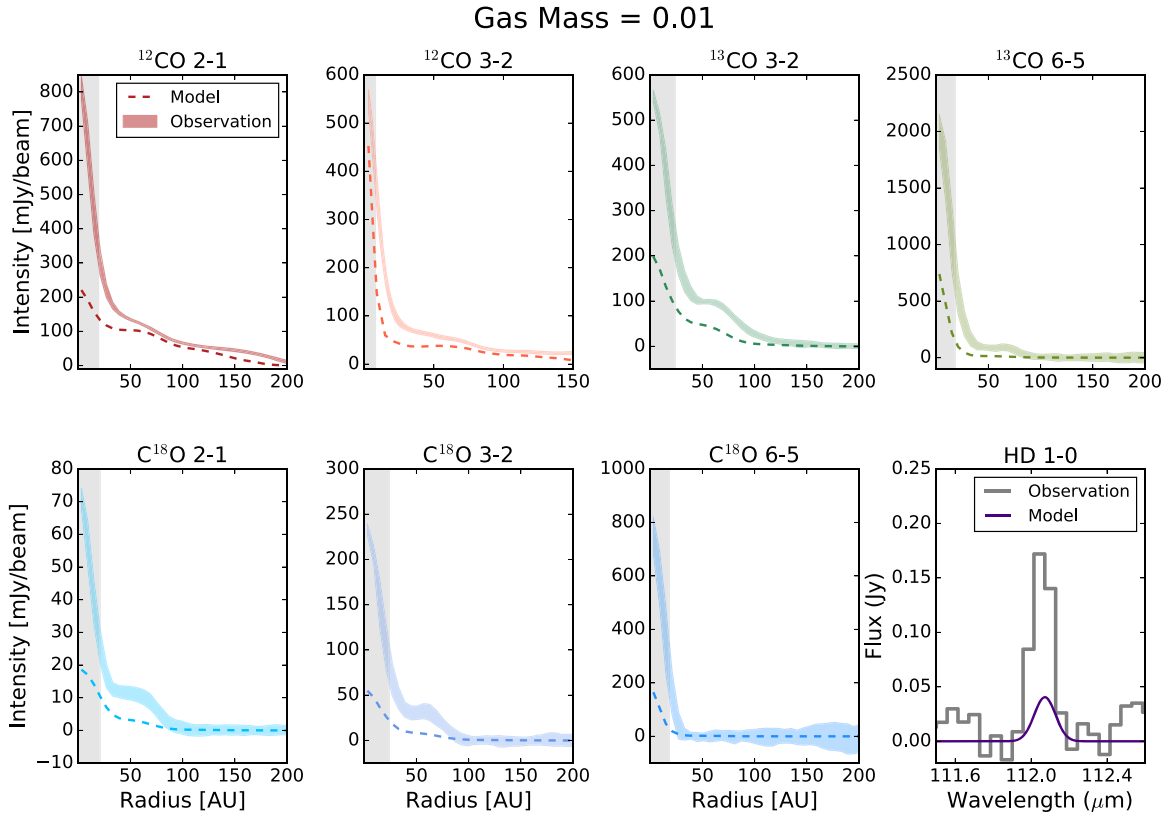


**Figure A6.** Integrated intensity profiles of observations and a model based on the initial model (Figure A1) but with a gas mass equal to 0.01 $M_{\odot}$.

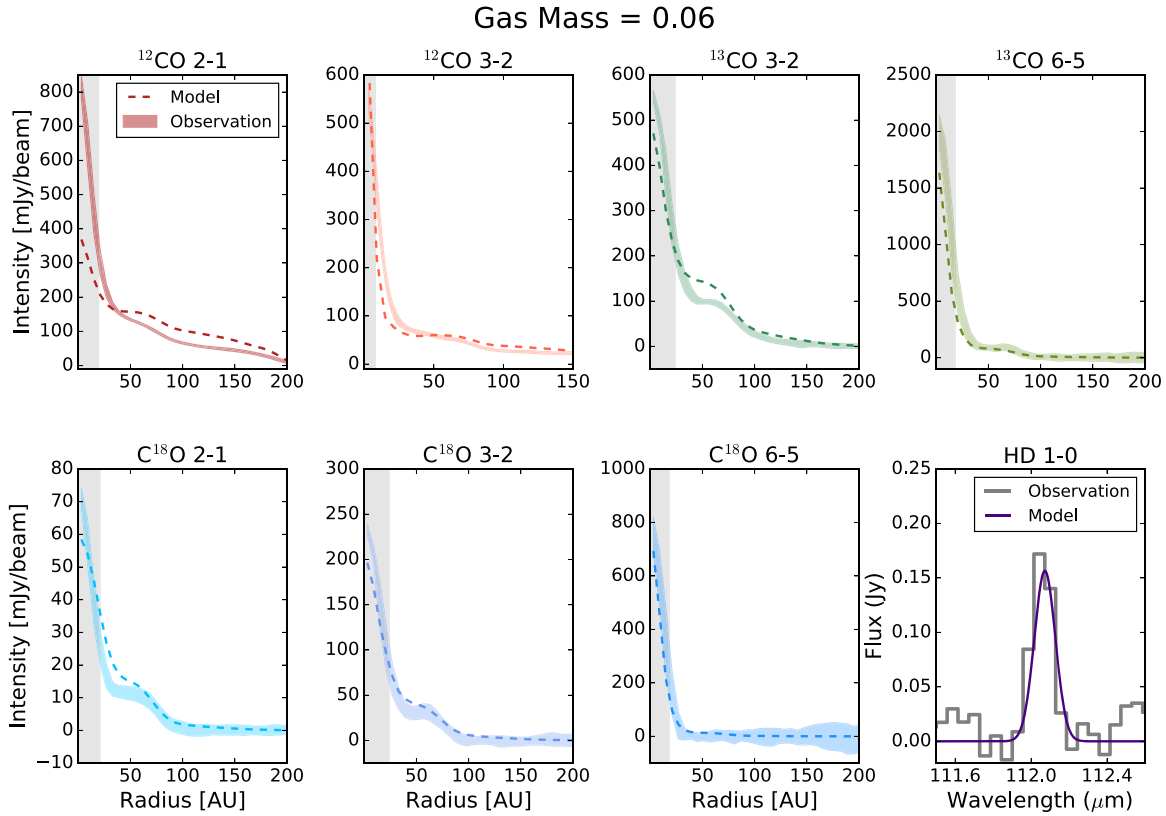


**Figure A7.** Integrated intensity profiles of observations and a model based on the initial model (Figure A1) but with a gas mass equal to 0.06 $M_{\odot}$.

### *A.3. Gas Mass*

An increase in the total gas mass increases the intensity from each line along all radii (see Figures A6 and A7). A higher gas mass results in a higher column density for each molecule, and some of the CO lines (especially $^{12}$CO 2–1) are already optically thick in explored mass range. There are also isotopologues whose emission is not fully optically thick in the lower-mass models; thus, changes in their column have a strong effect on their flux. Increasing the gas mass from 0.01 to 0.02 $M_{\odot}$ doubles the peak integrated flux in C$^{18}$O, creates a 25% increase in $^{13}$CO and $^{12}$CO 3–2, and an creates an increase of ∼20% in $^{12}$CO 2–1. Our best-fit model has a disk mass of 0.025 $M_{\odot}$. We arrived at this value only after the gas and small dust components of our model were given different $\Psi$ values. With a gas mass of 0.05 $M_{\odot}$ and $\Psi_{\rm gas} = 1.1$ and $\Psi_{\rm smalldust} = 1.2$, the HD flux increases by a factor of two, and emission in CO at large radii also increases by a factor of 2–3 depending on the isotopologue. Due to this, a decrease in total gas mass is justified. Decreasing the mass to 0.023 $M_{\odot}$ brings the HD flux back down to what Herschel observed and brings the CO emission back down to values that agree with ALMA observations.

### *A.4. Small Dust Component Mass*

Given a constant gas mass of 0.05 $M_{\odot}$ and a starting small dust mass of $1.0 \times 10^{-4}$ $M_{\odot}$ or higher, decreasing the small dust mass has a similar effect to increasing gas mass (see Figures A8 and A9). At $1.0 \times 10^{-4}$ $M_{\odot}$ and lower, flux beyond 20 au increases at a faster rate than within 20 au, leading to exaggerated features, such as the plateaus in C$^{18}$O 2–1 and 3–2 becoming peaks at small dust masses less than $2.5 \times 10^{-5}$ $M_{\odot}$. The small dust population absorbs and scatters radiation and in some instances leads to a CO line profile that is extincted. Eliminating small dust allows for the gas that exists to emit more freely as a major opacity source is removed. The small dust mass is particularly impactful on the HD emission, because the small dust governs the propagation of UV radiation, with smaller dust masses allowing UV photons from the star to penetrate deeper layers of the disk, directly affecting the gas heating terms. This helps populate the HD $J = 1$ level, increasing the HD $J = 1$–0 line flux. In our final model, we were not strongly motivated to change the small dust mass beyond what had been initially predicted, but it could be a useful lever in future modeling of disks. At present the strongest constraint on the mass of the small dust is the SED and scattered-light emission from the surface.

### *A.5. $r_{\rm exp}$: Outer Tapering Radius*

At this specified radius the abundance of a component exponentially decreases. Altering the $r_{\rm exp}$ affects outer-disk emission, as it significantly depletes the corresponding component, as seen in Figures A10 and A11. It is only significant in $^{12}$CO 2–1 and 3–2, as these are the only intensity profiles with emission beyond 100 au. If the gas and small dust $r_{\rm exp}$ value becomes less than the large dust $r_{\rm exp}$, the effect is much stronger and acts similar to decreasing $\gamma$.

### *A.6. $h_c$: Characteristic Height*

An increase of the height of the disk results in an increase in intensity across all radii and in all molecules, with the ones most strongly affected being the least abundant (see Figures A12 and A13). A change in scale height increases the column that one observes, which then increases the flux of an optically thin molecule. However, this does not strongly

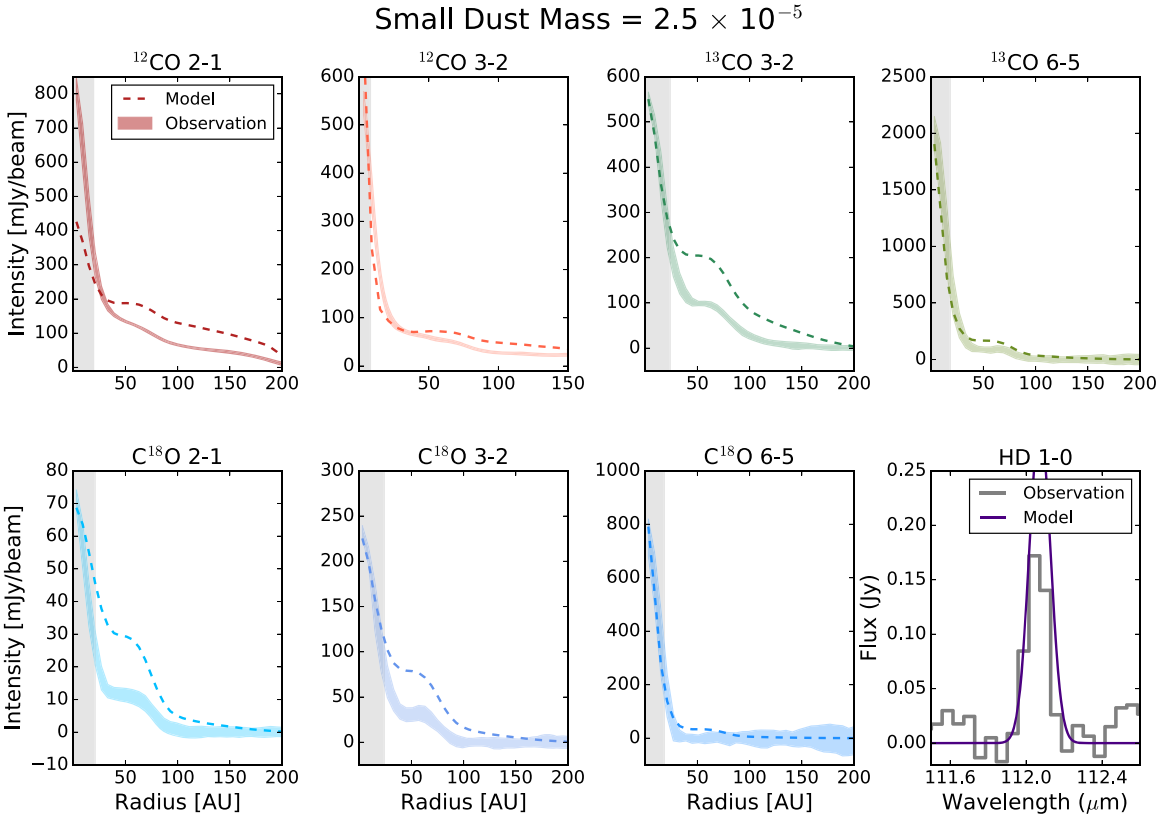


**Figure A8.** Integrated intensity profiles of observations and a model based on the initial model (Figure A1) but with a total small dust mass equal to $2.5 \times 10^{-5}\ M_{\odot}$.

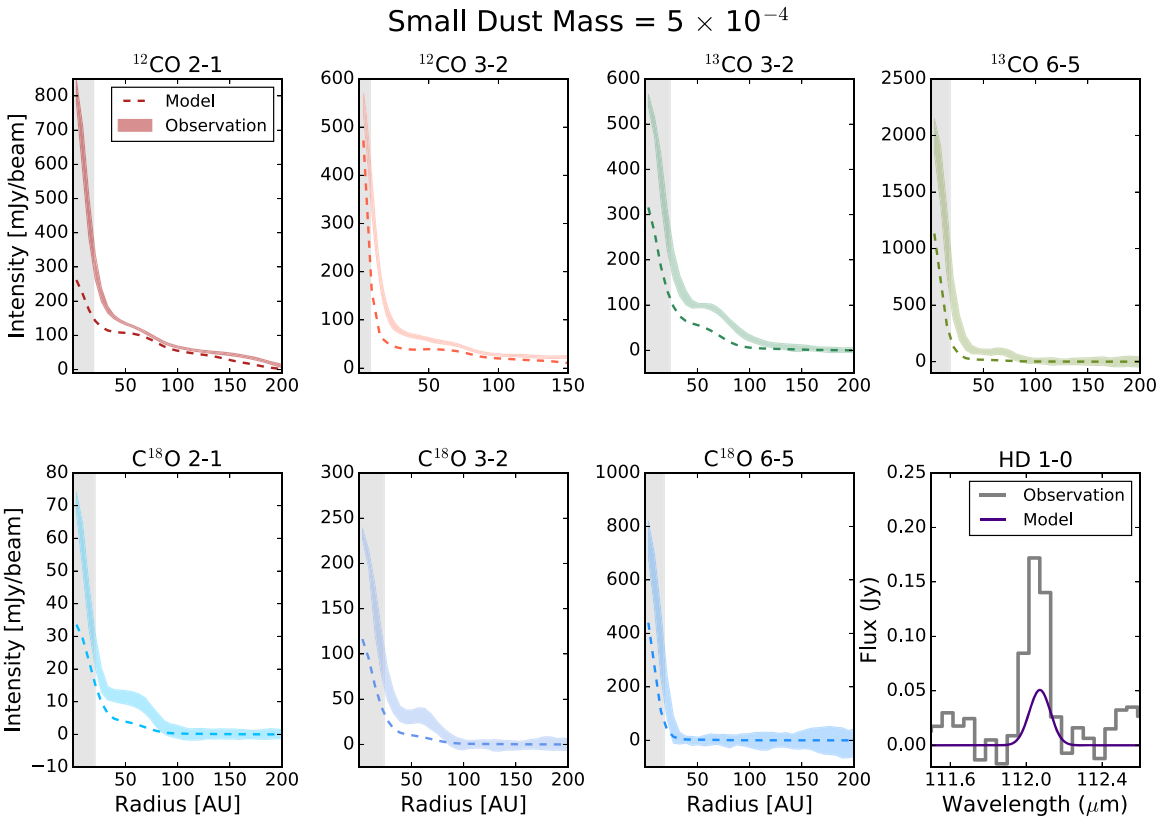


**Figure A9.** Integrated intensity profiles of observations and a model based on the initial model (Figure A1) but with a total small dust mass equal to $5 \times 10^{-4}\ M_{\odot}$.

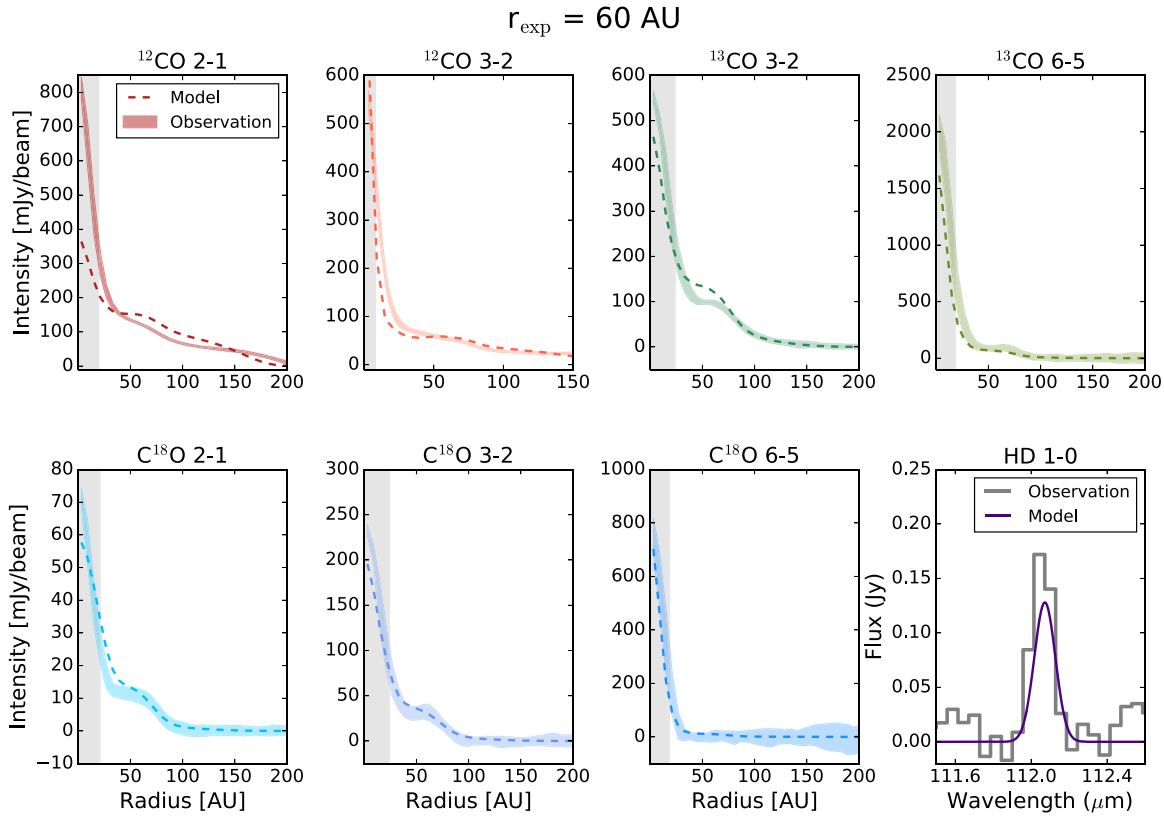


**Figure A10.** Integrated intensity profiles of observations and a model based on the initial model (Figure A1) but with $r_{\mathrm{exp_{out}}}$ in the gas and small dust = 60 au.

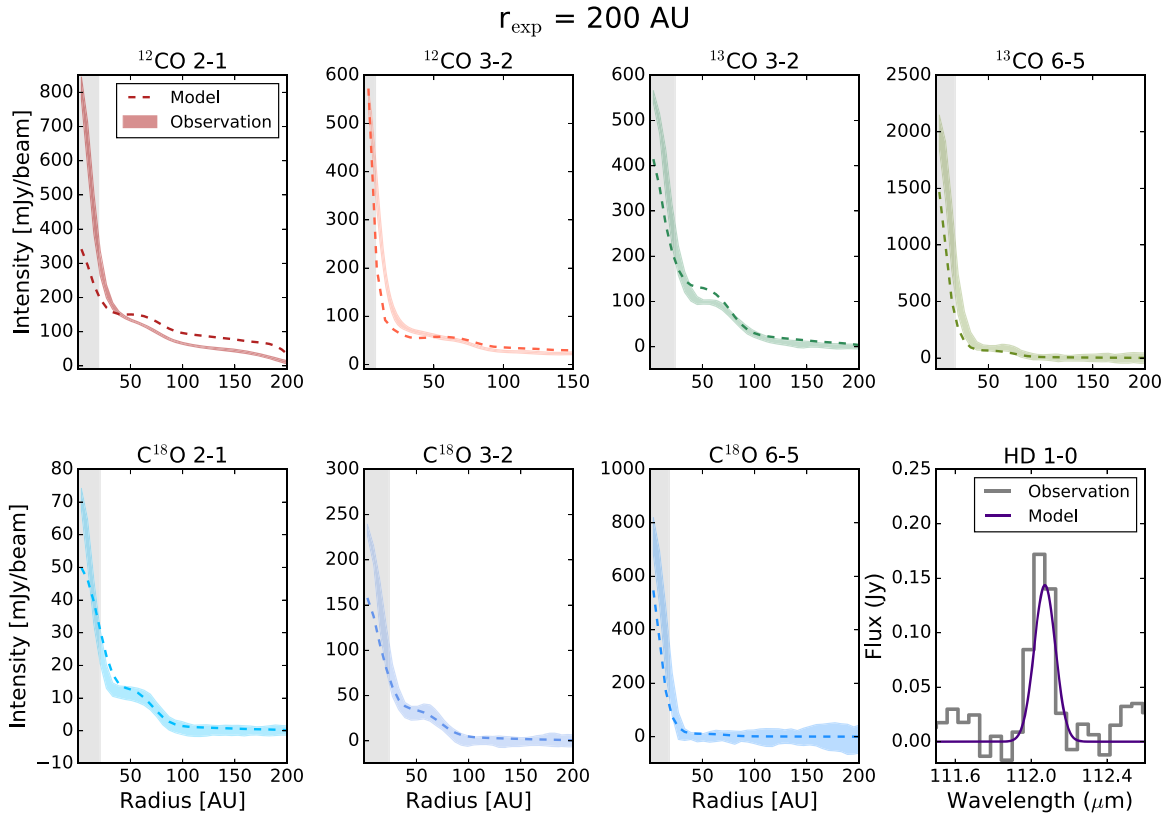


**Figure A11.** Integrated intensity profiles of observations and a model based on the initial model (Figure A1) but with $r_{\mathrm{exp_{out}}}$ in the gas and small dust = 200 au.

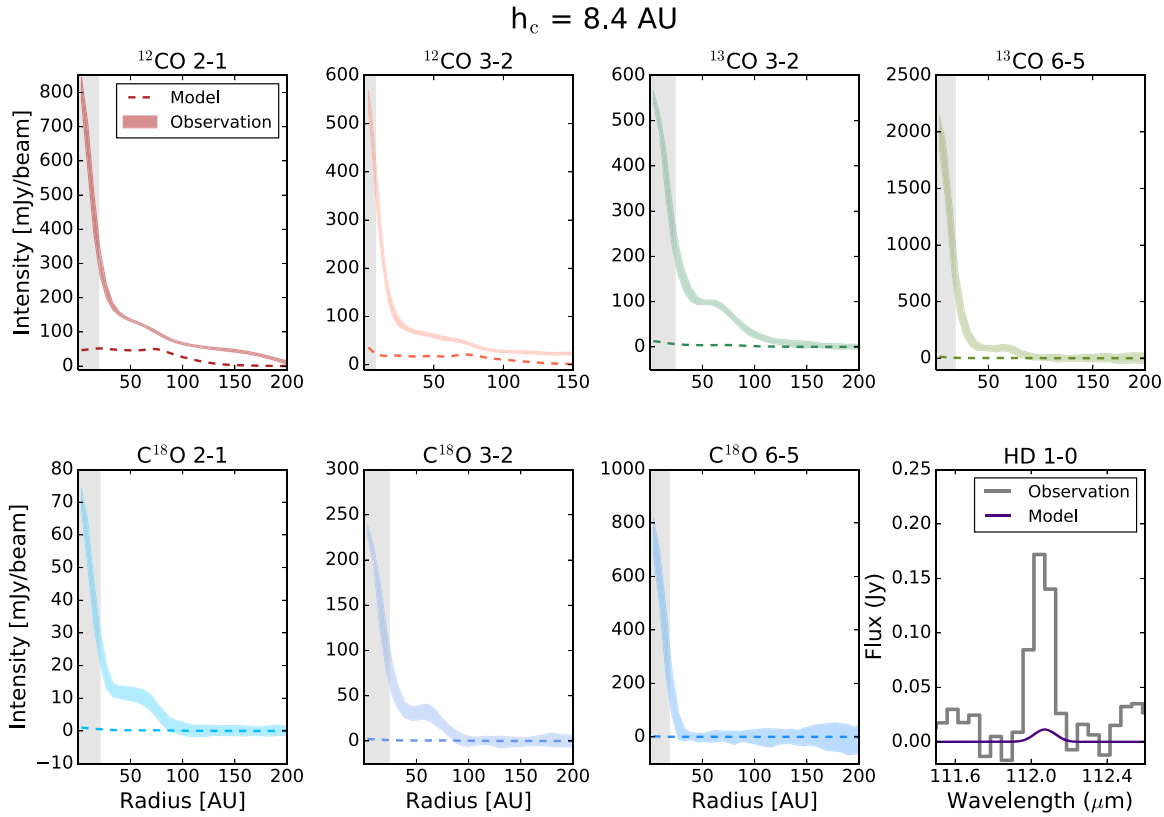


**Figure A12.** Integrated intensity profiles of observations and a model based on the initial model (Figure A1) but with $h_c$ in the gas and small dust = 8.4 au.

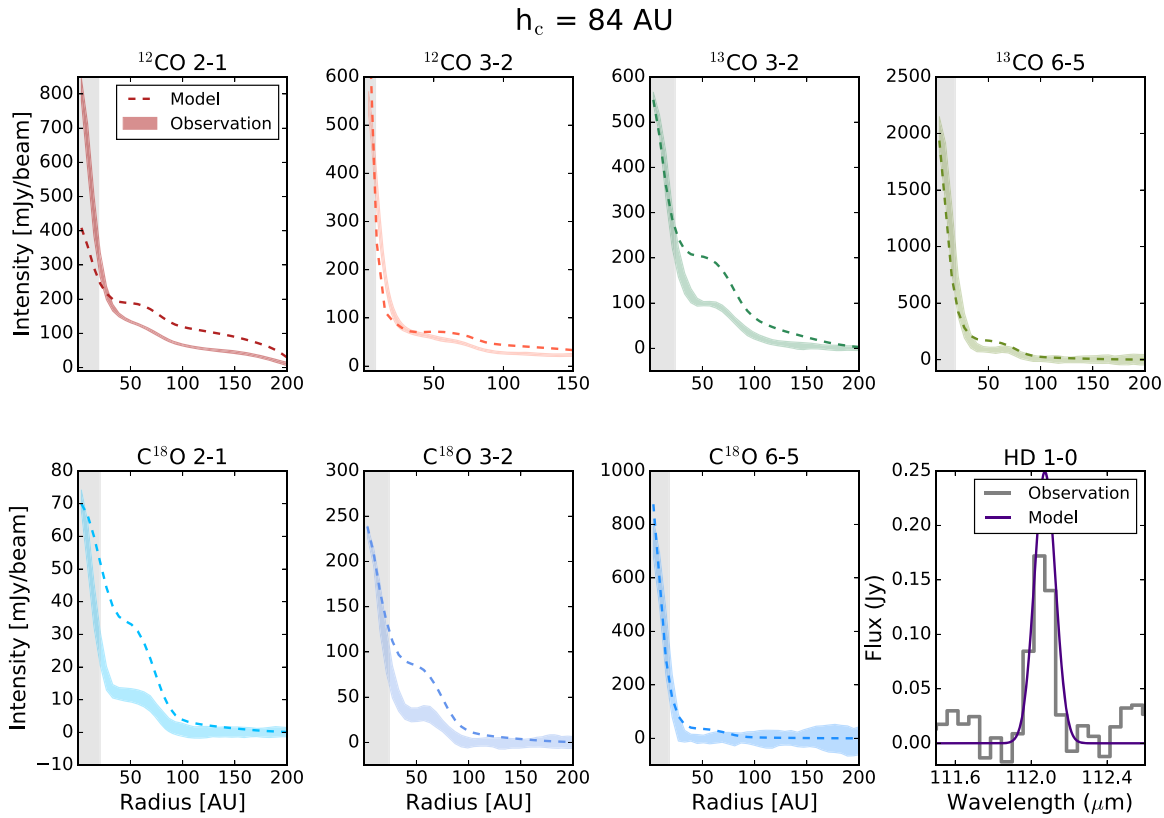


**Figure A13.** Integrated intensity profiles of observations and a model based on the initial model (Figure A1) but with $h_c$ in the gas and small dust = 84 au.

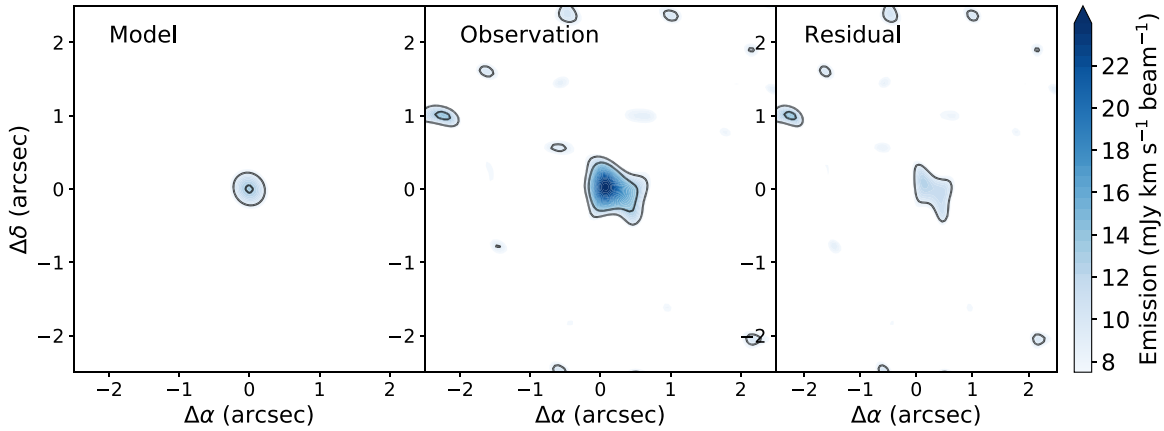


**Figure A14.** ALMA observation of $^{13}C^{18}O$ $J = 3$–2 line emission (middle panel) as compared to our final TW Hya modeled $^{13}C^{18}O$ $J = 3$–2 flux (left panel) and the residual (right panel). Contours trace the location of 9 and 13 mJy flux values.

affect optically thick molecules. An increase of two times the scale height only results in a ∼5% increase in peak intensity in $^{12}CO$ 2–1 and a full 20% increase in the least common isotopologue transition considered here, $C^{18}O$ 6–5.

The scale height, scale radius, Ψ, and $\gamma$ of the large dust population do not have strong effects on the CO line profiles. The temperature of the star also does not have a strong effect; a change in 1000 K resulted in only a 1% increase across all lines.

The parameters we find having the largest impact on the CO and HD flux were gas mass, the flaring parameter Ψ, surface density distribution parameter $\gamma$, and small dust mass. The gas mass affects all CO lines and has a stronger influence on the optically thin lines. Ψ and $\gamma$ both redistribute flux between the inner and outer regions of the disk depending on where the majority of the gas component is located. The small dust mass was not a parameter that needed to be altered from its initial value, but it has a strong effect on the HD flux and could be utilized in future studies as long as the SED is taken into account.

## ORCID iDs

Jenny K. Calahan https://orcid.org/0000-0002-0150-0125
Edwin Bergin https://orcid.org/0000-0003-4179-6394
Ke Zhang https://orcid.org/0000-0002-0661-7517
Richard Teague https://orcid.org/0000-0003-1534-5186
Ilsedore Cleeves https://orcid.org/0000-0003-2076-8001
Jennifer Bergner https://orcid.org/0000-0002-8716-0482
Geoffrey A. Blake https://orcid.org/0000-0003-0787-1610
Paolo Cazzoletti https://orcid.org/0000-0002-1917-7370
Viviana Guzmán https://orcid.org/0000-0003-4784-3040
Michiel R. Hogerheijde https://orcid.org/0000-0001-5217-537X
Jane Huang https://orcid.org/0000-0001-6947-6072
Mihkel Kama https://orcid.org/0000-0003-0065-7267
Ryan Loomis https://orcid.org/0000-0002-8932-1219
Karin Öberg https://orcid.org/0000-0001-8798-1347
Charlie Qi https://orcid.org/0000-0001-8642-1786
Ewine F. van Dishoeck https://orcid.org/0000-0001-7591-1907
Jeroen Terwisscha van Scheltinga https://orcid.org/0000-0002-3800-9639
Catherine Walsh https://orcid.org/0000-0001-6078-786X
David Wilner https://orcid.org/0000-0003-1526-7587

## References

Aikawa, Y., van Zadelhoff, G. J., van Dishoeck, E. F., & Herbst, E. 2002, A&A, 386, 622
Andrews, S. M. 2020, ARA&A, 58, 483
Andrews, S. M., Czekala, I., Wilner, D. J., et al. 2010, ApJ, 710, 462
Andrews, S. M., Wilner, D. J., Hughes, A. M., et al. 2012, ApJ, 744, 162
Ansdell, M., Williams, J. P., van der Marel, N., et al. 2016, ApJ, 828, 46
Bailer-Jones, C. A. L., Rybizki, J., Fouesneau, M., Mantelet, G., & Andrae, R. 2018, AJ, 156, 58
Bergin, E. A., & Cleeves, L. I. 2018, in Chemistry During the Gas-Rich Stage of Planet Formation, ed. H. J. Deeg & J. A. Belmonte (Berlin: Springer), 137
Bergin, E. A., Cleeves, L. I., Gorti, U., et al. 2013, Natur, 493, 644
Bergin, E. A., & Williams, J. P. 2017, ASSL, 445, 1
Birnstiel, T., Klahr, H., & Ercolano, B. 2012, A&A, 539, A148
Bisschop, S. E., Fraser, H. J., Öberg, K. I., van Dishoeck, E. F., & Schlemmer, S. 2006, A&A, 449, 1297
Bosman, A. D., Walsh, C., & van Dishoeck, E. F. 2018, A&A, 618, A182
Brickhouse, N. S., Cranmer, S. R., Dupree, A. K., Luna, G. J. M., & Wolk, S. 2010, ApJ, 710, 1835
Bruderer, S. 2013, A&A, 559, A46
Bruderer, S., Doty, S. D., & Benz, A. O. 2009, ApJS, 183, 179
Bruderer, S., van Dishoeck, E. F., Doty, S. D., & Herczeg, G. J. 2012, A&A, 541, A91
Calvet, N., D'Alessio, P., Hartmann, L., et al. 2002, ApJ, 568, 1008
Cleeves, L. I., Bergin, E. A., Qi, C., Adams, F. C., & Öberg, K. I. 2015, ApJ, 799, 204
Cleeves, L. I., Öberg, K. I., Wilner, D. J., et al. 2018, ApJ, 865, 155
Cutri, R. M., Skrutskie, M. F., van Dyk, S., et al. 2003, 2MASS All Sky Catalog of Point Sources (Washington, DC: NASA)
Debes, J. H., Jang-Condell, H., Weinberger, A. J., Roberge, A., & Schneider, G. 2013, ApJ, 771, 45
Du, F., & Bergin, E. A. 2014, ApJ, 792, 2
Dullemond, C. P., & Dominik, C. 2004, A&A, 421, 1075
Dullemond, C. P., Juhasz, A., Pohl, A., et al. 2012, RADMC-3D: A Multi-purpose Radiative Transfer Tool, Astrophysics Source Code Library, v2.0, ascl:1202.015
Eistrup, C., Walsh, C., & van Dishoeck, E. F. 2018, A&A, 613, A14
Favre, C., Cleeves, L. I., Bergin, E. A., Qi, C., & Blake, G. A. 2013, ApJ, 776, L38
Fayolle, E. C., Balfe, J., Loomis, R., et al. 2016, ApJL, 816, L28
Fedele, D., van Dishoeck, E. F., Kama, M., Bruderer, S., & Hogerheijde, M. R. 2016, A&A, 591, A95
Fraser, H. J., Collings, M. P., McCoustra, M. R. S., & Williams, D. A. 2001, MNRAS, 327, 1165
Frerking, M. A., Langer, W. D., & Wilson, R. W. 1982, ApJ, 262, 590
Gaia Collaboration, Brown, A. G. A., Vallenari, A., et al. 2018, A&A, 616, A1
Gorti, U., Hollenbach, D., Najita, J., & Pascucci, I. 2011, ApJ, 735, 90
Hartmann, L., Megeath, S. T., Allen, L., et al. 2005, ApJ, 629, 881
Hayashi, C. 1981, PThPS, 70, 35
Huang, J., Andrews, S. M., Cleeves, L. I., et al. 2018, ApJ, 852, 122
Kama, M., Bruderer, S., van Dishoeck, E. F., et al. 2016, A&A, 592, A83
Kama, M., Trapman, L., Fedele, D., et al. 2020, A&A, 634, A88

Kenyon, S. J., & Hartmann, L. 1995, ApJS, 101, 117
Krijt, S., Ormel, C. W., Dominik, C., & Tielens, A. G. G. M. 2016, A&A, 586, A20
Krijt, S., Schwarz, K. R., Bergin, E. A., & Ciesla, F. J. 2018, ApJ, 864, 78
Lacy, J. H., Knacke, R., Geballe, T. R., & Tokunaga, A. T. 1994, ApJL, 428, L69
Lacy, J. H., Sneden, C., Kim, H., & Jaffe, D. T. 2017, ApJ, 838, 66
Linsky, J. L. 1998, SSRv, 84, 285
Long, F., Herczeg, G. J., Pascucci, I., et al. 2017, ApJ, 844, 99
Low, F. J., Smith, P. S., Werner, M., et al. 2005, ApJ, 631, 1170
Lynden-Bell, D., & Pringle, J. E. 1974, MNRAS, 168, 603
Mathis, J. S., Rumpl, W., & Nordsieck, K. H. 1977, ApJ, 217, 425
McClure, M. K., Bergin, E. A., Cleeves, L. I., et al. 2016, ApJ, 831, 167
McMullin, J. P., Waters, B., Schiebel, D., Young, W., & Golap, K. 2007, in ASP Conf. Ser. 376, Astronomical Data Analysis Software and Systems XVI, ed. R. A. Shaw, F. Hill, & D. J. Bell (San Francisco, CA: ASP), 127
Mekkaden, M. V. 1998, A&A, 340, 135
Miotello, A., Bruderer, S., & van Dishoeck, E. F. 2014, A&A, 572, A96
Miotello, A., van Dishoeck, E. F., Kama, M., & Bruderer, S. 2016, A&A, 594, A85
Miotello, A., van Dishoeck, E. F., Williams, J. P., et al. 2017, A&A, 599, A113
Müller, H. S. P., Schlöder, F., Stutzki, J., & Winnewisser, G. 2005, JMoSt, 742, 215
Öberg, K. I., & Bergin, E. A. 2016, ApJL, 831, L19
Öberg, K. I., Murray-Clay, R., & Bergin, E. A. 2011, ApJL, 743, L16
Pinte, C., Ménard, F., Duchêne, G., et al. 2018, A&A, 609, A47
Poglitsch, A., Waelkens, C., Geis, N., et al. 2010, A&A, 518, L2
Qi, C., Ho, P. T. P., Wilner, D. J., et al. 2004, ApJL, 616, L11
Qi, C., Öberg, K. I., Andrews, S. M., et al. 2015, ApJ, 813, 128
Reboussin, L., Wakelam, V., Guilloteau, S., Hersant, F., & Dutrey, A. 2015, A&A, 579, A82
Richards, S. N., Moseley, S. H., Stacey, G., et al. 2018, JAI, 7, 1840015
Röllig, M., & Ossenkopf, V. 2013, A&A, 550, A56
Rosenfeld, K. A., Andrews, S. M., Hughes, A. M., Wilner, D. J., & Qi, C. 2013, ApJ, 774, 16
Rothman, L. S., Jacquemart, D., Barbe, A., et al. 2005, JQSRT, 96, 139
Schoonenberg, D., & Ormel, C. W. 2017, A&A, 602, A21
Schwarz, K. R., Bergin, E. A., Cleeves, L. I., et al. 2016, ApJ, 823, 91
Schwarz, K. R., Bergin, E. A., Cleeves, L. I., et al. 2019, ApJ, 877, 131
Shakura, N. I., & Sunyaev, R. A. 1973, A&A, 500, 33
Stevenson, D. J., & Lunine, J. I. 1988, Icar, 75, 146
Teague, R., Bae, J., & Bergin, E. A. 2019, Natur, 574, 378
Teague, R., & Foreman-Mackey, D. 2018, RNAAS, 2, 173
Thi, W. F., Mathews, G., Ménard, F., et al. 2010, A&A, 518, L125
Trapman, L., Miotello, A., Kama, M., van Dishoeck, E. F., & Bruderer, S. 2017, A&A, 605, A69
van Boekel, R., Henning, T., Menu, J., et al. 2017, ApJ, 837, 132
van Zadelhoff, G. J., van Dishoeck, E. F., Thi, W. F., & Blake, G. A. 2001, A&A, 377, 566
Visser, R., van Dishoeck, E. F., & Black, J. H. 2009, A&A, 503, 323
Weintraub, D. A., Masson, C. R., & Zuckerman, B. 1989a, ApJ, 344, 915
Weintraub, D. A., Sandell, G., & Duncan, W. D. 1989b, ApJL, 340, L69
Weintraub, D. A., Saumon, D., Kastner, J. H., & Forveille, T. 2000, ApJ, 530, 867
Wilner, D. J., Bourke, T. L., Wright, C. M., et al. 2003, ApJ, 596, 597
Wilner, D. J., Ho, P. T. P., Kastner, J. H., & Rodríguez, L. F. 2000, ApJL, 534, L101
Wilson, T. L. 1999, RPPh, 62, 143
Woitke, P., Kamp, I., Antonellini, S., et al. 2019, PASP, 131, 064301
Woitke, P., Kamp, I., & Thi, W. F. 2009, A&A, 501, 383
Woodall, J., Agúndez, M., Markwick-Kemper, A. J., & Millar, T. J. 2007, A&A, 466, 1197
Woods, P. M., & Willacy, K. 2009, ApJ, 693, 1360
Zhang, K., Bergin, E. A., Blake, G. A., Cleeves, L. I., & Schwarz, K. R. 2017, NatAs, 1, 0130
Zhang, K., Bergin, E. A., Schwarz, K. R., Krijt, S., & Ciesla, F. 2019, ApJ, 883, 98
Zhang, K., Blake, G. A., & Bergin, E. A. 2015, ApJL, 806, L7
Zhang, K., Bosman, A. D., & Bergin, E. A. 2020a, ApJL, 891, L16
Zhang, K., Pontoppidan, K. M., Salyk, C., & Blake, G. A. 2013, ApJ, 766, 82
Zhang, K., Schwarz, K. R., & Bergin, E. A. 2020b, ApJL, 891, L17
Zhu, Z., Zhang, S., Jiang, Y.-F., et al. 2019, ApJL, 877, L18